Typeset using L A T E X twocolumn style in AASTeX63

Farbod Jahandar, René Doyon, Étienne Artigau, Neil Cook, Charles Cadieux, David Lafrenière, Thierry Forveille, Jean-François Donati, Pascal Fouqué, Andrés Carmona, et al.

Draft version April 3, 2024
Typeset using LaTeX **twocolumn** style in AASTeX63

Comprehensive High-resolution Chemical Spectroscopy of Barnard's star with SPIRou

Farbod Jahandar [1], René Doyon [1,2], Étienne Artigau [1,2], Neil J. Cook [1], Charles Cadieux [1], David Lafrenière [1], Thierry Forveille [3], Jean-François Donati [4], Pascal Fouqué [5,4], Andrés Carmona [3], Ryan Cloutier [6], Paul Cristofari [7], Eric Gaidos [8], João Gomes da Silva [9], Lison Malo [1,2], Eder Martioli [10,11], J.-D. do Nascimento, Jr. [12,7], Stefan Pelletier [1], Thomas Vandal [1], and Kim Venn [13]

[1] *Trottier Institute for Research on Exoplanets, Département de Physique, Université de Montréal, 1375 Ave Thérèse-Lavoie-Roux, Montréal, QC, H2V 0B3, Canada*
[2] *Observatoire du Mont-Mégantic, Université de Montréal, Montréal H3C 3J7, Canada*
[3] *Univ. Grenoble Alpes, CNRS, IPAG, 38000 Grenoble, France*
[4] *Université de Toulouse, CNRS, IRAP, 14 Avenue Belin, 31400 Toulouse, France*
[5] *Canada-France-Hawaii Telescope, CNRS, Kamuela, HI 96743, USA*
[6] *Department of Physics & Astronomy, McMaster University, 1280 Main St W, Hamilton, ON L8S 4L8, Canada*
[7] *Center for Astrophysics | Harvard & Smithsonian, 60 Garden Street, Cambridge, MA, 02138, USA*
[8] *University of Hawai'i at Mānoa, Department of Earth Sciences, Honolulu, HI 96822, USA*
[9] *Instituto de Astrofísica e Ciências do Espaço, Universidade do Porto, CAUP, Rua das Estrelas, 4150-762, Porto, Portugal*
[10] *Laboratório Nacional de Astrofísica, Rua Estados Unidos 154, 37504-364, Itajubá - MG, Brazil*
[11] *Institut d'Astrophysique de Paris, CNRS, UMR 7095, Sorbonne Université, 98 bis bd Arago, 75014 Paris, France*
[12] *Universidade Federal do Rio Grande do Norte (UFRN), Departamento de Física, 59078-970, Natal, RN, Brazil*
[13] *Department of Physics and Astronomy, University of Victoria, Victoria, BC, V8W 3P2, Canada*

(Received September 12, 2023; Revised February 27, 2024; Accepted March 4, 2024)

ABSTRACT

Determination of fundamental parameters of stars impacts all fields of astrophysics, from galaxy evolution to constraining the internal structure of exoplanets. This paper presents a detailed spectroscopic analysis of Barnard's star that compares an exceptionally high-quality (an average signal-to-noise ratio of ∼1000 in the entire domain), high-resolution NIR spectrum taken with CFHT/SPIRou to PHOENIX-ACES stellar atmosphere models. The observed spectrum shows thousands of lines not identified in the models with a similar large number of lines present in the model but not in the observed data. We also identify several other caveats such as continuum mismatch, unresolved contamination and spectral lines significantly shifted from their expected wavelengths, all of these can be a source of bias for abundance determination. Out of $> 10^4$ observed lines in the NIR that could be used for chemical spectroscopy, we identify a short list of a few hundred lines that are reliable. We present a novel method for determining the effective temperature and overall metallicity of slowly-rotating M dwarfs that uses several groups of lines as opposed to bulk spectral fitting methods. With this method, we infer $T_{\rm eff} = 3231 \pm 21$ K for Barnard's star, consistent with the value of 3238 ± 11 K inferred from the interferometric method. We also provide abundance measurements of 15 different elements for Barnard's star, including the abundances of four elements (K, O, Y, Th) never reported before for this star. This work emphasizes the need to improve current atmosphere models to fully exploit the NIR domain for chemical spectroscopy analysis.

Keywords: Stars: low-mass — M dwarfs — stellar atmosphere — fundamental parameters — atmospheres

1. INTRODUCTION

Corresponding author: Farbod Jahandar
farbod.jahandar@umontreal.ca

M dwarfs are the most common type (Henry et al. 1994; Winters et al. 2019; Reylé et al. 2021) of stars in the Galaxy. The determination of fundamental parameters of M dwarfs impacts many fields of astrophysics, from the study of the chemical evolution of stars to the internal modeling of their potential exoplanets' interior structure. The typical mass and radius of M dwarfs lie within 0.1-0.74 $M_\odot$ and 0.1-0.67 $R_\odot$ (Mann et al. 2015; Reiners et al. 2018) making them the smallest types of stars in the main sequence. As an immediate result of their low mass and almost fully convective nature, the hydrogen-burning timescale in M dwarfs can be much longer than the age of the Universe, often several hundred Gyr depending on the mass of the star (Chabrier & Baraffe 2000). The small size and low luminosity of M dwarfs, result in their habitable zone being much closer to the star. Consequently, planets within this habitable zone naturally have shorter orbital periods, which makes them ideal targets for searching and characterizing HZ exoplanets via transit (e.g., Muirhead et al. 2014; Martinez et al. 2017) and radial velocity methods (Campbell et al. 1988; Latham et al. 1989; Mayor & Queloz 1995). Occurrence rate studies (e.g., Bonfils et al. 2013; Dressing & Charbonneau 2015; Mulders et al. 2015; Gaidos et al. 2016; Cloutier & Menou 2020; Hsu et al. 2020) have also shown that M dwarfs host more short-period planets than more massive stars, and the Kepler mission's observations have revealed the planet occurrence rate of 2.5 ± 0.2 planets per M dwarf for the targets with radii 1-4 $R_\oplus$ and period < 200 days (Dressing & Charbonneau 2015).

Various methods have been used for determining the fundamental parameters of stars. The effective temperature ($T_{\rm eff}$) is determined through medium- and high-resolution spectroscopy (e.g., Lamb et al. 2016; Rajpurohit et al. 2018), photometry (e.g., Casagrande et al. 2008) as well as the bolometric method involving interferometric measurements of the stellar radius (Boyajian et al. 2012). While the interferometry method is arguably the most accurate way of determining $T_{\rm eff}$ independent of synthetic models, measuring angular diameters is only feasible for the nearest M dwarfs given the maximum baselines of current optical/infrared interferometers. Photometry also has its caveats. Even with the best photometric calibrations, photometric estimates of $T_{\rm eff}$ of some M dwarfs can show up to 2σ offset from spectroscopic values (Souto et al. 2020). These challenges emphasize the need for other complementary estimates inferred from high-resolution spectroscopy.

The spectroscopy method is also not without challenges. Due to the low surface temperature of M dwarfs (i.e., $2500\,{\rm K} < T_{\rm eff} < 4000\,{\rm K}$), their spectra are generally dominated by the extensive blends of molecular bands (e.g., TiO, VO, OH, CO, H_2O) and absorption lines that make the detection of the continuum level of the spectrum difficult. Nevertheless, a compelling reason for conducting spectroscopy in the NIR rather than in the optical is that it is where most of the stellar flux is concentrated for M dwarfs. The current state-of-the-art of synthetic models such as PHOENIX (Allard et al. 2012) combined with the recent advances in high-resolution NIR spectroscopy offer a new opportunity for the determination of the stellar parameters and elemental abundances of M dwarfs.

Some of the previous spectroscopic works such as Rojas-Ayala et al. (2010), Rajpurohit et al. (2018), Marfil et al. (2021) and Cristofari et al. (2022a) have characterized M dwarfs through high-resolution spectroscopy using synthetic models. However, the currently popular synthetic models, specially for cool stars like M dwarfs, are incomplete and, up to a noticeable level inaccurate (Blanco-Cuaresma 2019). A few examples of such incompleteness in the current synthetic spectra are the lack of identification of many observed atomic and molecular features due to incomplete line lists and inaccurate line-formation for weak lines in the synthetic spectra (Önehag et al. 2012). High-resolution spectroscopy on M dwarfs is the first step to improving the theoretical base of synthetic spectra via a detailed comparison between the data and the models.

This paper presents the chemical spectroscopy of Barnard's star observed by the SPIRou instrument. This includes a high-resolution spectral analysis and examination of over 18000 absorption lines and molecular bands. We describe the observations with SPIRou in Section 2. The remaining bulk of the paper focuses on three subjects. First, in Section 3, we examine the caveats of one of the best synthetic spectra for M dwarfs by giving a detailed comparison of the discrepancies between the data and the models. Second, in Section 4, we present a new method for determining the effective temperature and metallicity of M dwarfs that minimizes uncertainties inherent to the PHOENIX-ACES synthetic models. In Section 5, we report the chemical abundance of 15 different elements for Barnard's star, and discuss potential reasons behind discrepancies in the reported abundances in the literature. This analysis is followed by concluding remarks in Section 6.

2. OBSERVATIONS

SPIRou (SpectroPolarimètre InfraRouge, Donati et al. 2020) is a near-infrared spectropolarimeter on the Canada-France-Hawaii Telescope (CFHT) that provides simultaneous high-resolution (R$\sim$70000) NIR spectra in

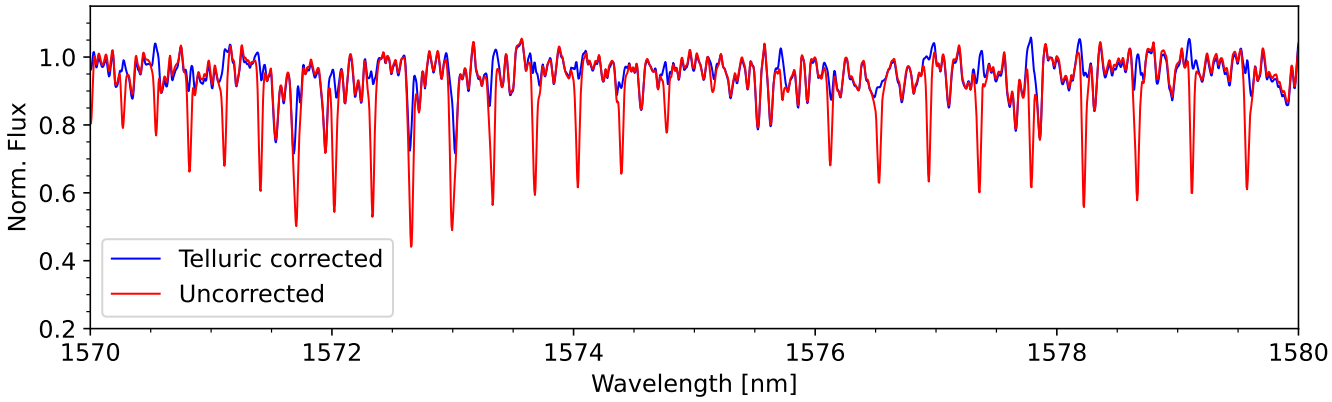

Figure 1. Spectral comparison showcasing the impact of telluric correction for a single visit. The red spectrum illustrates the uncorrected spectrum, while the blue one represents the spectrum after telluric correction using APERO (Cook et al. 2022).

the $YJHK$ bands between 0.97 and 2.49 μm. This wavelength interval includes some of the common spectral metallicity indicators in M dwarfs (e.g., Ca I triplet and Na I doublet; Rojas-Ayala et al. 2010; Veyette et al. 2016) as well as hundreds of known absorption lines that can be used for better determination of metallicity, $\log g$ and $T_{\rm eff}$. SPIRou was specifically designed for the detection of exoplanets via precision velocimetry (1–2 m/s) with unique polarimetric capability that enables measurements of the surface magnetic field of stars. Barnard's star (Gl 699), one of the closest and brightest M dwarf (d = 1.8 pc), is one of SPIRou's radial velocity standards regularly observed as part of the SPIRou Legacy Survey[1] (SLS, Donati et al. 2020). The stellar properties of Barnard's star are given in Table 1. The spectrum presented here results from the median co-addition of 846 visits secured between 2018 and 2023, enabling exceptionally high SNR (∼1000). Each visit consisted of a polarimetric sequence comprising four consecutive 60 s exposures each observed in a different polarization state. The observations were reduced using APERO (A PipelinE to Reduce Observations; Cook et al. 2022) that provides full calibration, extraction, and telluric correction, enabling corrections at the m/s precision level, with the maximum telluric residual of $<1\%$ of the continuum level in the combined spectrum (see Figure 1).

Of prime importance in our analysis is the spectral fidelity on a spectral scale of a few resolution elements. A spurious telluric residual signal could affect a line measurement for example. The spectrum analyzed here is the median combination of observations obtained at barycentric velocities spanning the full yearly excursions for that star (±26.5 km/s) and thus any telluric residual would be practically eliminated from the final spectrum.

3. SYNTHETIC SPECTRA

The chemical spectroscopic analysis of Barnard's star's spectrum was carried out using the PHOENIX-ACES models[2] (Allard et al. 2012; Husser et al. 2013). These synthetic spectra are generated using the precomputed model grids from the PHOENIX radiative transfer code (Allard & Hauschildt 1996; Hauschildt et al. 1997; Allard et al. 2003). PHOENIX models are based on certain radiative transfer assumptions such as the convection process via the mixing length theory, hydrostatic equilibrium, and Local Thermodynamic Equilibrium (LTE) systems (Allard & Hauschildt 1996). By comparing synthetic spectra from the PHOENIX grid, we find that these models resemble our observed spectrum reasonably well[3] (see Figure 2) except for the discrepancies described in Section 3.1. This includes an excellent reproduction of both isolated absorption lines and molecular bands such as OH, CO, and CN.

The spectral sampling of PHOENIX-ACES synthetic spectra varies between 0.01-0.04 Å from the Y to the K band. We convolve PHOENIX-ACES models to the same spectral resolution of SPIRou by creating an instrumental Line Spread Function (LSF). This LSF is then applied across a range of velocity bins, with the LSF recalculated for each bin to ensure accurate representation of variations across the wavelength grid. This

[1] The SLS is one of CFHT's large programs and it focuses on exoplanet detection and characterization and magnetic fields of young M stars.

[2] PHOENIX version of 16.01.00B, released on 2012-02-11

[3] For further details, see Figures B.1 to B.5 in the appendix for the full spectral comparison, and Table A.1 containing the normalized fluxes of the observed data and a synthetic model analogous to Barnard's star.

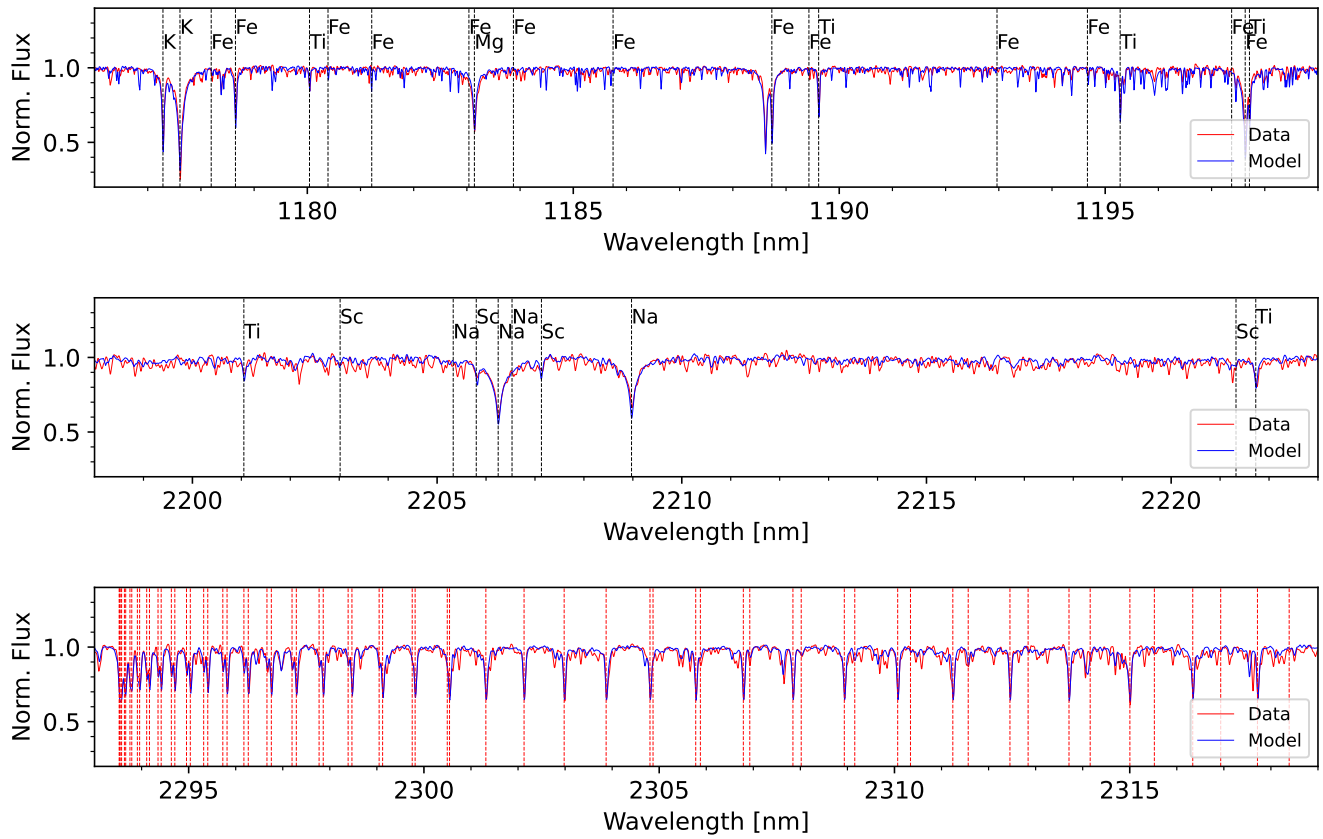

Figure 2. Comparison between the observed data (red) and the model (blue) with $T_{\rm eff}$, $\log g$, and metallicity of 3200 K, 5.0 dex and −0.5 dex, respectively. The *Top panel* shows some alpha elements (e.g., Ti I and Mg I) as well as several isolated and blended Fe I lines. The *middle panel* shows the Na I doublet frequently used in several studies as metallicity indicators of M dwarfs. The *bottom panel* shows numerous absorption features of the CO band head starting around 2.29 μm (red dashed lines).

process effectively matches the spectral resolution of the models to that of SPIRou.

Next, we utilized the iSpec tool (Blanco-Cuaresma et al. 2014; Blanco-Cuaresma 2019) to normalize the convolved synthetic spectra. This tool first detects spectral peaks using a maximum filter, then filters out strong spectral lines and outliers, and further smoothens the data with a median filter. After these filtering steps, a cubic spline model is fitted to the continuum. This method effectively divided out the overall spectral energy distribution (SED), allowing for the isolation of specific spectral features. By performing this process all at once (and not order-based), a robust and consistent fit across the entire spectrum was ensured. The observed data was also normalized using the same method, ensuring consistency in the treatment of both synthetic and observed spectra.

3.1. *Comparison Between the Data and the Model*

While there is an overall consistency between the model and the data (see Figure 2), not all features in the observed spectrum exist in the synthetic model with $T_{\rm eff}$ of 3200 K, $\log g$ of 5.0 and [M/H] of −0.5 dex, which are close to the stellar parameters of Barnard's star generally adopted in the literature (e.g., Mann et al. 2015; Artigau et al. 2018). Our analysis (see Table 2) has revealed that there are over 18600 features in Barnard's star spectrum but only 6849 of those are identified in the model, assuming the following two selection criteria: 1) only lines with a minimum line depth of 5% from the continuum level are considered and 2) the central wavelength of a given line measured from both the observed spectrum and the synthetic model are within one resolution element (assuming the spectral resolution of 70000)

Inconsistencies between the observed spectrum and synthetic model are discussed below.

3.1.1. *Continuum mismatch*

In about 5% of the spectrum (mainly between 985-1068 nm), there is an apparent mismatch between the normalized continuum level of the data and the model. As shown in Figure 3, while the exact locations of FeH lines in the Y band are projected correctly in the model,

Table 1. Barnard's star (Gl 699) stellar properties

Parameter	Value	Ref.
Designations		
TIC	325554331	1
2MASS	J17574849+0441405	2
UCAC4	474-068224	3
Gaia DR3	4472832130942575872	4
Astrometry		
RA (J2016.0)	17:57:48.50	4
DEC (J2016.0)	+04:41:36.11	4
$\mu_\alpha \cos\delta$ (mas/yr)	-801.551 ± 0.032	4
μ_δ (mas/yr)	10362.394 ± 0.036	4
π (mas)	546.9759 ± 0.0401	4
Distance (pc)	1.8282 ± 0.0001	4
Stellar parameters		
$T_{\rm eff}$ (K)	3231 ± 21	5
[M/H]	-0.48 ± 0.04	5
[Fe/H]	-0.39 ± 0.03	5
SpT	M4.2	6
$M_\star$ ($M_\odot$)	0.159 ± 0.016	6
$R_\star$ ($R_\odot$)	0.1869 ± 0.0012	6
$\log g$ (dex)	5.08 ± 0.15	7
$L_\star$ ($L_\odot$)	0.00342 ± 0.00003	6
Photometry		
V	9.540 ± 0.031	8
R	8.315 ± 0.012	8
I	6.730 ± 0.020	8
g	10.428 ± 0.020	8
r	8.913 ± 0.011	8
i	7.508 ± 0.013	8
J	5.244 ± 0.020	2
H	4.834 ± 0.034	2
$K_{\rm s}$	4.524 ± 0.020	2
Rotation		
Rotation Period (days)	145 ± 15	9
$v \sin i$ ($\rm kms^{-1}$)	< 2	10

References—1. TIC (Stassun et al. 2019) 2. 2MASS (Skrutskie et al. 2006) 3. UCAC4 (Zacharias et al. 2013) 4. *Gaia* EDR3 (Vallenari et al. 2021) 5. This work 6. Mann et al. (2013) 7. Maldonado et al. (2020) 8. Synthetic photometry (Mann et al. 2015) 9. Toledo-Padrón et al. (2019) 10. Reiners et al. (2018)

there is a noticeable difference between the continuum levels. A similar effect is also observed in Lim et al. (2023), when they compared PHOENIX models with the JWST spectra. This discrepancy is not necessarily unique to the FeH bands, as there are some unaffected FeH lines in the H band, but we empirically observed more severe mismatches around the molecular bands of the Y band. This problem causes an overestimate for $T_{\rm eff}$ and an underestimate for metallicity. Because of this issue, all spectral features between 985-1068 nm were excluded in the abundance analysis presented later.

3.1.2. *Unidentified lines in the models*

Several thousand absorption features in the spectrum are absent from the default line list of PHOENIX (see Figure 4), hence these lines are not used in the model. While some of these unknown features were independently examined by different research groups (e.g., FeH lines by Hargreaves et al. 2010 and Souto et al. 2017), or detected using the laboratory-based NIST line list database (NIST 2019), there are still a significant number of unidentified spectral features in all the $YJHK$ bands.

3.1.3. *Line shifts*

As shown in Figure 5, some of the spectral features, usually associated with molecules, are shifted (typically less then 5 km/s). Similar discrepancy was also reported in other studies such as Tannock et al. (2022). A likely explanation for these shifts is an inherent wavelength uncertainty with the line list used in the synthetic spectra, however, this requires further investigations. These empirical shifts must be taken into account in the analysis for determining abundances and the effective temperature.

4. SPECTRAL ANALYSIS

A χ^2 minimization technique is the core of the spectral fitting procedure used in this paper. The stellar parameters ($T_{\rm eff}$ and the overall metallicity) of the synthetic spectra are varied and matched to the observed spectrum until convergence (minimal χ^2) is reached. However, it is important to note that this χ^2 minimization is not performed over the entire wavelength domain at once. Instead, the process is conducted iteratively over subsets of small spectral regions, the specifics of which will be defined later in the following sections.

In practice, multiple synthetic spectra from the PHOENIX-ACES grid were generated with $T_{\rm eff}$ between 2300 K and 4300 K (typical temperature range of M dwarfs) and with overall metallicity ranging from -1.5 to 0.5 dex in 0.5 dex increments. This metallicity range was chosen to cover the majority of the metallicities previously reported for Barnard's star; the range spans from -0.86 dex (Marfil et al. 2021) to 0.61 dex (Passegger et al. 2021). Next, a fixed $\log g$ of 5.0 dex was used for all our

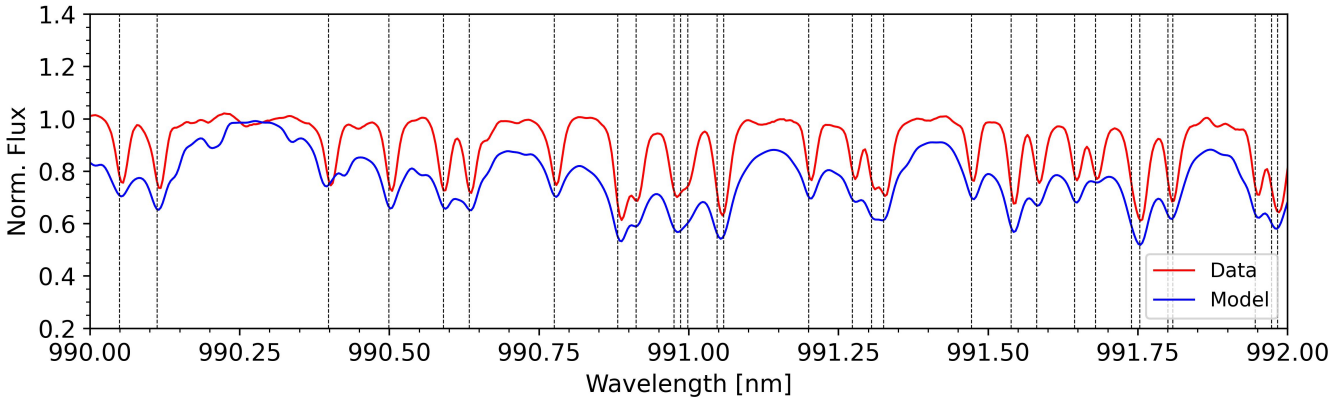

Figure 3. Example of a spectral domain with strong continuum discrepancy between the model (blue) and the data (red). The black dotted lines show the wavelengths of FeH lines. The same model as in Figure 2 was used.

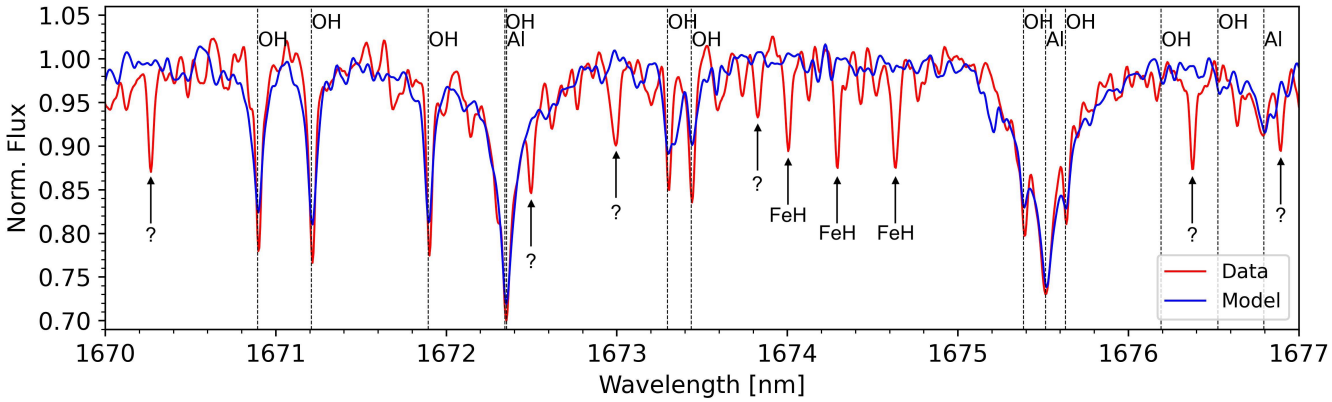

Figure 4. Example of a spectral region showing clear absorption features (red) not present in the model (blue). Some of these lines, such as FeH lines, have been previously examined by Hargreaves et al. 2010 and Souto et al. 2017. The arrows with question marks show a few examples of unidentified lines out of thousands in the full wavelength range. The same model as in Figure 2 was used.

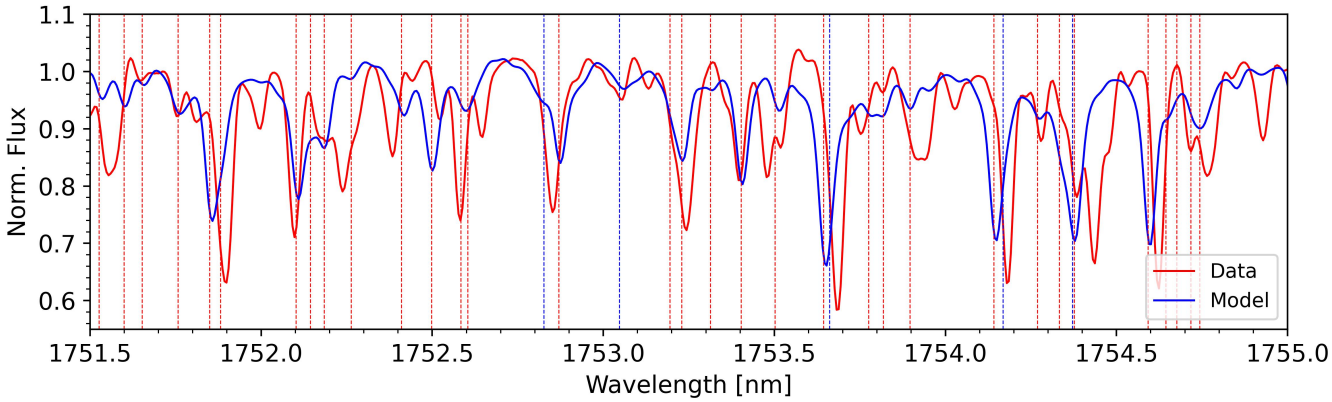

Figure 5. Spectral region featuring several water and OH lines. There are multiple red and blue shifts between the data (red) and the model (blue). The red and blue vertical dashed lines represent the location of H_2O and OH lines from the PHOENIX line list. The same model as in Figure 2 was used.

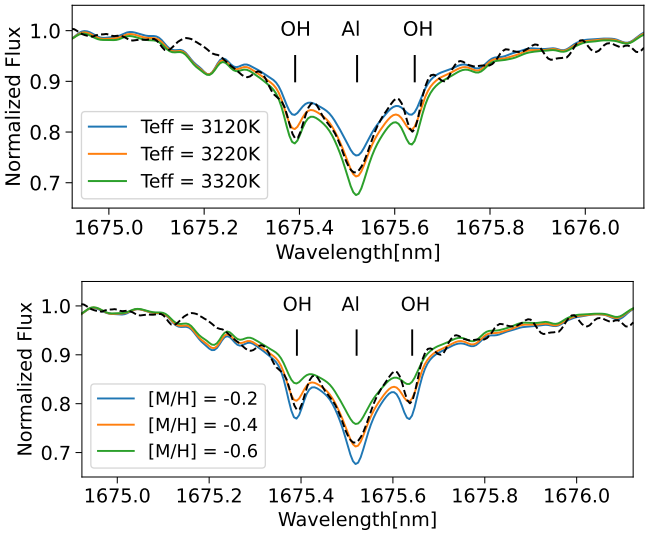

Figure 6. SPIRou observation of the Al I line (1675.514 nm) of Barnard's star (black dashed line). *Top panel*: The solid lines represent the ACES models for a fixed metallicity of −0.4 dex and $T_{\rm eff}$ values of 3120 K, 3220 K, and 3320 K. *Bottom panel*: Same as top panel, but the ACES models have a fixed $T_{\rm eff}$ = 3220 K and metallicity values of −0.6 dex, −0.4 dex and −0.2 dex. These plots illustrate the sensitivity of NIR high-resolution spectroscopy for constraining both the metallicity and effective temperature of M dwarfs.

models, consistent with the mean and standard deviation of the reported $\log g$ values for Barnard's star in SIMBAD (Wenger et al. 2000), 4.98 ± 0.21 dex.

Additionally we empirically confirmed that a variation in $\log g$ within the range of 5.0 ± 0.2 dex has a negligible effect on our analysis, and majority of the literature values for $\log g$ are within this range. The relative insensitivity of the synthesized spectra to this parameter makes small offsets between the true and assumed values acceptable (well within our reported errors), thus the fixed value of $\log g$ does not affect our results. Furthermore, by fixing $T_{\rm eff}$ and $\log g$ values determined independently, we can minimize additional uncertainties resulting from degeneracies in line shapes caused by various combinations of $T_{\rm eff}$, $\log g$, and metallicity.

The final χ^2 fitting was performed on a finer grid of models, with 20 K and 0.1 dex increments for the $T_{\rm eff}$ and metallicity, respectively, all bi-linearly interpolated from the main pre-computed spectral grid (see Figure 6).

4.1. *Line Selection*

Line selection is a key component of any spectral analysis mainly for two reasons. First, as we have shown, since synthetic models do not perfectly match the observed data, choosing spectral domains with good agreement between observations and models yields better results less susceptible to systematic effects. Moreover, different spectral features do not behave in the same way with the variation of physical parameters of the star, therefore, it is important to choose spectral features that are highly sensitive to the changes in the spectral parameter that is being measured. For instance, OH lines are much less sensitive to effective temperature variation compared to H_2O molecular bands, meaning that for a fixed metallicity, the depth of the H_2O lines changes more significantly compared to OH lines for different $T_{\rm eff}$ (Souto et al. 2017). Similarly, Fe I and Fe II lines have traditionally been used to constrain $\log g$ due to their different sensitivities to variations in $\log g$ (Takeda et al. 2002).

There are thousands of spectral features in the data and the synthetic spectra. Given the significant discrepancies between the model and the data (see Section 3.1), blind spectral fitting to derive the stellar parameters and chemical abundances is not the best approach. As shown

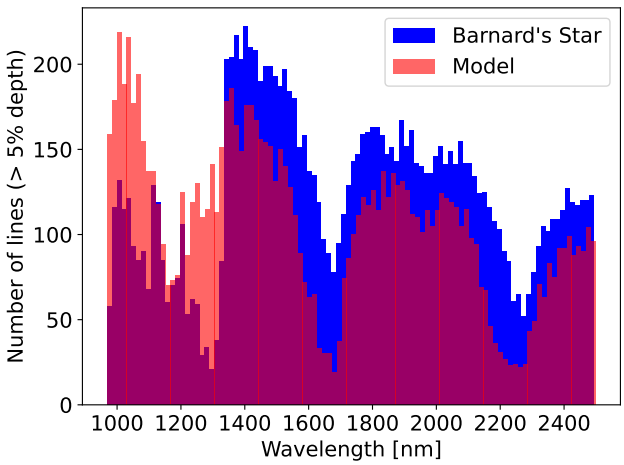

Figure 7. Comparison between the number of lines in the observed data (blue) and the synthetic model (red) with a similar $T_{\rm eff}$, $\log g$ and metallicity.

in Figure 7, and noted by Artigau et al. (2018), there are hundreds of spectral features missing in the H and K bands of a synthetic model with similar properties to that of Barnard's star. This is the reverse situation in the Y and J bands for which the model predicts numerous strong lines that are clearly not observed. To avoid any bias toward the known and unknown caveats of the synthetic spectra, we developed a pipeline to find only those features that are common to both the data and the model. A spectral line is chosen only if it satisfies the following criteria:

1. an observed line is present in the model

Table 2. Line selection statistics

Condition	Model (# of lines)	Data (# of lines)	Common lines (# of lines)
Depth of +1% cont. level	18926	18617	11155
Depth of +5% cont. level (criteria 1 & 2, see Section 4.1)	13303	12522	6849
Depth of +5% cont. level (criteria 1 to 5, see Section 4.1) - exist at $T_{\rm eff}$ = 3200†	–	–	1593
Depth of +5% cont. level (criteria 1 to 5, see Section 4.1) - exist regardless of $T_{\rm eff}$*	–	–	636
Depth of +5% cont. level (all criteria in Section 4.1 and Section 4.3)$^{\hat{}}$	–	–	210

NOTE— † The spectral features that exist in the data and a model with the effective temperature of 3200 K, which is similar to Barnard's star's $T_{\rm eff}$.
* The spectral features that exist in the data and models with the $T_{\rm eff}$ range between 3000 K and 4200 K. This is the final list used for determining the $T_{\rm eff}$.
$^{\hat{}}$ This is the final list used for determining the chemical abundances.

2. the line depth is greater than 5% from the continuum level[4],
3. no continuum mismatch between model and observations (see Section 3.1.1)
4. the central wavelength from both the observed spectrum and the synthetic model do not differ more than one resolution element
5. the lines that have a potential source of contamination or saturation (e.g.,nearby lines such as H_2O or OH lines), within half a resolution element, are flagged

Using the above criteria, 1593 spectral features are identified from both the data and the synthetic model with $T_{\rm eff}$ of 3200 K, and log g of 5.0 dex. However, for the purpose of $T_{\rm eff}$ measurements, to avoid any line selection bias from the prior choice of 3200 K for the model used for the line selection, we added another filter to pick only those lines that exist in the data and models regardless of the $T_{\rm eff}$ of the star. More specifically, we selected the features that exist in models with $T_{\rm eff}$ range between 3000 K and 4000 K and with line depth of 5% or more. The final result is a total of 636 spectral features, that are in both the observed data and the synthetic model regardless of the stellar $T_{\rm eff}$ (see Table 2).

4.2. *Group Determination of Effective Temperature*

There is a significant variation of 3092 K (Hojjatpanah et al. 2019) to 3463 K (Fouqué et al. 2018) for $T_{\rm eff}$ of Barnard's star from previous studies. One of the plausible reasons behind such a variation in spectroscopic $T_{\rm eff}$ is the choice of spectral features. We investigated this by a bulk line-by-line $T_{\rm eff}$ determination on all 636 matched spectral features as a function of wavelength. In this method, we created multiple groups of spectral features that exist in both the data and the models, each containing several absorption lines or molecular bands (typically 20). It is important to note that these lines are not always adjacent to one another in the spectrum. Their specific separation can vary, depending on the location of the next matching line between the model and the data, and are not constrained to a fixed value. We do not include the full spectral range from the first to the last line in a group; rather, our methodology involves a more targeted approach. Around each absorption line, we apply masking to isolate a subsection of the spectrum, specifically encompassing the closest local minima around each spectral line. This approach allows us to focus our analysis on the most relevant spectral features while avoiding potential noise or interference from less meaningful portions of the spectrum. Then each group is analyzed independently through a χ^2 fitting routine to infer both $T_{\rm eff}$ and [M/H] for all groups. The heart of this method is determining $T_{\rm eff}$ as a function of wavelength for different fixed metallicities. In each scenario, the metallicity is fixed to minimize the effect of unusually high or low abundance lines and only focus on the overall metallicity. In Figure 8, three cases of $T_{\rm eff}$ vs wavelength for the three fixed metallicities of −1.0, −0.4, and 0 dex are shown. The $T_{\rm eff}$ determined from H and K bands changes in opposite directions when the metallicity increases. We created a graph of $T_{\rm eff}$ dispersion with different wave-

[4] The telluric correction were done with the maximum residual level of well bellow 1% in the combined spectrum, which is significantly smaller than our 5% depth thresholds.

length regions as a function of metallicity in Figure 9. The advantage of this method is that it yields several independent measurements that can be used to characterize the inherent uncertainties associated with the fitting procedure. As shown in Figure 9, the $\sigma_{T_{\rm eff}}$ of a given $T_{\rm eff}$ shows a minimum with metallicity, allowing to constrain both $T_{\rm eff}$ and [M/H]. This analysis applied to Barnard's star spectrum yields $T_{\rm eff} = 3231 \pm 21$ K and $[{\rm M/H}] = -0.40 \pm 0.05$, in good agreement with the previous literature values (Mann et al. 2013; Gaidos et al. 2014; Gaidos & Mann 2014; Maldonado et al. 2020). Note that this is different from the overall metallicity listed in Table 1, that is determined via line-by-line fitting of different elements (will be discussed in Section 4.3).

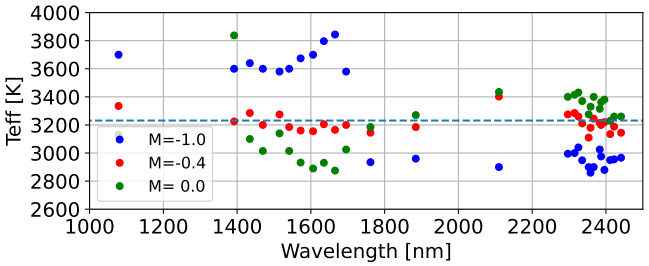

Figure 8. $T_{\rm eff}$ vs wavelength for three different fixed overall metallicities. There is a strong correlation and anti-correlation between the estimated $T_{\rm eff}$ for each scenario. The smaller the $T_{\rm eff}$ variation is between different bands, the closer the model is to the data. The dashed line shows the average of $T_{\rm eff}$ for the best fit.

Multiple points in this $T_{\rm eff}$ line-by-line map have to be addressed. First, nearly all of the Y and J bands are excluded in this analysis partially due to the mentioned continuum mismatch of molecular bands (e.g., FeH bands) in these regions (see Section 3.1.1). The synthetic models systematically overestimate the depth of the majority of the FeH lines. Therefore, using the molecular bands in the Y and J bands causes a significant overestimation of $T_{\rm eff}$. The reason is that for most of the Y and J bands, for a fixed metallicity, the hotter a star, the weaker the depth and equivalent width of molecular and atomic lines are. Therefore, the model has to increase the $T_{\rm eff}$ to compensate for the continuum mismatch between the data and the model. Moving toward the H and K bands, the estimated $T_{\rm eff}$ values are fairly consistent around 3200 K.

4.3. *Abundance Determination*

For this work, we generated a master line list by combining the most recent available line list used for Bt-Settl PHOENIX models (Allard et al. 2010) and the

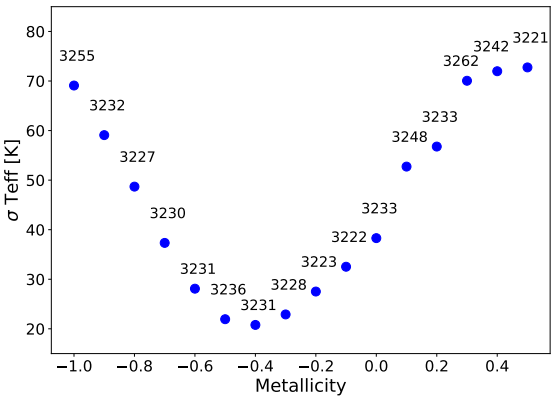

Figure 9. $T_{\rm eff}$ dispersion for different fixed overall metallicities. The average $T_{\rm eff}$ of each case is above each circle and its internal uncertainty is shown in the y-axis. The lowest variation corresponds to the metallicity of -0.40 ± 0.05 and $T_{\rm eff}$ of 3231 ± 21 K. At this metallicity $T_{\rm eff}$ values for different wavelengths have the lowest amount of variation between different spectral bands (see Figure 8). Note that the variation in $T_{\rm eff}$ is calculated as the standard deviation divided by $\sqrt{N-1}$, where N represents the number of groups of individual lines used in this analysis.

atomic database of the National Institute of Standards and Technology (NIST 2019). These line lists contain a collection of atomic and molecular transition parameters, including the exact wavelength location of various atoms and molecules. While we used all 636 spectral features for the $T_{\rm eff}$ determination, for the chemical abundance analysis, we took the conservative approach of selecting only atomic lines and OH lines. It is important to note that since the abundance of hydrogen is not modified when we change the overall metallicity of the models, the OH abundance from the best-fit model can represent the oxygen abundance. We excluded all non-OH molecular lines such as H_2O, FeH, TiO, and CO lines. H_2O is very sensitive to $T_{\rm eff}$ variations, unlike OH; therefore, minor inaccuracies in the fixed $T_{\rm eff}$ can significantly misestimate any oxygen abundance inferred from H_2O lines. In section 3.1.1, we showed that our synthetic models suffer from continuum mismatch in most of the Y band, which has a significant concentration of FeH lines. While there are some FeH lines in other bands, for consistency and due to the discrepancies with FeH lines in the Y band, we decided to infer the iron abundance directly from the Fe I lines only. For other multi-metal molecules like TiO and CO, since we have control only over the overall metallicity in our synthetic models, properly disentangling the individual contributions of each molecule to the entire line is not feasible. Additionally, we removed ionized spectral features, as

this work focuses solely on the chemical abundance of the neutral lines. Excluding all the mentioned spectral features, we selected 210 spectral features that are suitable for line-by-line chemical spectroscopy. Note that the wavelength spacing between two consecutive lines is often too small for the resolution of our spectrum (e.g., in some cases it was as small as 0.2 resolution element of our data). In these cases, we carefully flagged all known spectral features within half a resolution element of each line and labeled it as a "Nearby Line" (see Appendix A).

To minimize the human bias in the selection and analysis process, all line selection criteria described above are applied automatically. However, a few of the weaker lines still needed direct supervision for further confirmation to use them in the analysis. To make this quantifiable, we used all the available lines of hydroxyl molecules (OH) to determine the optimal threshold for the depth of the spectral lines that can be used in the automatic pipeline. By measuring the abundance of OH as the function of the depth of the lines (see Figure 10), we concluded that all lines with a depth of less than 15% from the continuum level require extra supervision as some of them are not reliable for precise chemical spectroscopy. This extra supervision includes confirmation of consistent continuum level of nearby lines between the data and the model.

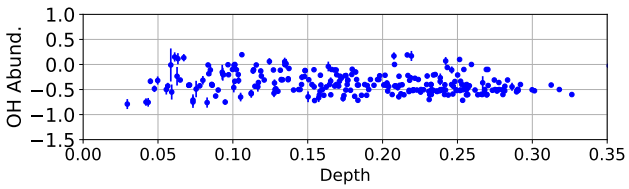

Figure 10. OH abundance as the function of line's depth. There is a correlation between each measurement's uncertainty (determined via MC sampling) and the depth of the line.

The abundance of a given element was determined by averaging the abundances from all its lines, based on the best fit from synthetic models. The uncertainties are the standard errors derived from the dispersion in the data for elements with more than two lines, otherwise an uncertainty of 0.12 dex per line is adopted which is the value inferred empirically from the numerous OH lines (see Figure 11). The solar normalized abundances of 15 different elements are reported in Table 3 and Figure 12. This work provides new abundance measurements for four elements: K, O, Y, and Th.

In addition to the individual element abundances, two different integrated abundances are determined: the overall metallicity, [M/H], and the alpha abundance,

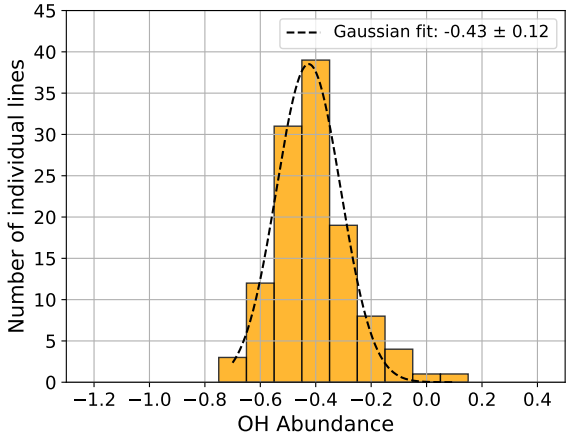

Figure 11. Distribution of OH abundance from 118 independent measurements of the OH lines that followed the five selection criteria of Section 4.1.

[α/H]. The overall metallicity ([M/H]) is defined as the average of the abundance of each element with the uncertainty expressed as the standard deviation of all values divided by $\sqrt{N-1}$, where N represents the number of different elements. This approach is chosen to avoid putting too much weight on the oxygen abundance characterized by a small uncertainty and to capture the observed dispersion from element to another. Note that for every spectral features, 50 Monte Carlo (MC) independent realizations of the observed spectrum are performed (see Appendix A for the MC errors) using the error for each pixel from the root-mean-square of the 846 spectra. This is done to better quantify the systematic uncertainty associated with our spectral fitting procedure. Since the spectrum of Barnard's star has a very high SNR, typical MC uncertainties are much smaller that the real dispersion inferred from several measurements of a given element.

The alpha elements require special attention as they play a significant role in better understanding of not only the star itself but also the interior structure of their potential rocky exoplanet, in particular, the refractory elements such as Mg and Si, that constitute the bulk material of a terrestrial exoplanet's core and mantle. In this work, we define the overall alpha abundance, or [α/H], as the average abundance of all alpha elements detected in the spectrum, namely: Mg, O, Si, Ca and Ti. The Ti abundance is directly measured from the Ti I lines. We specifically avoided using the titanium oxide (TiO) spectral lines in the analysis to ensure that our results are not influenced or skewed by the contribution of oxygen in these molecules. The oxygen abundance

Table 3. Stellar abundance of Barnard's star with respect to the Sun for various chemical species measured by SPIRou

[X/H]	This Work	# lines	Maldonado et al. (2020)	Ishikawa et al. (2022)
Fe I	-0.38 ± 0.03	29	-0.28 ± 0.04	-0.60 ± 0.18
Mg I	-0.33 ± 0.15	3	-0.34 ± 0.07	-0.52 ± 0.35
Ti I	-0.49 ± 0.03	18	-0.08 ± 0.05	-0.56 ± 0.30
Cr I	-0.47 ± 0.06	8	-0.27 ± 0.05	-0.70 ± 0.14
Na I	-0.68 ± 0.06	4	-0.16 ± 0.04	-0.61 ± 0.27
Ca I	-0.60 ± 0.12	2	-0.21 ± 0.06	-0.68 ± 0.13
Al I	-0.40 ± 0.06	4	-0.19 ± 0.06	–
Si I	-0.66 ± 0.12	1	-0.05 ± 0.05	–
C I	-0.56 ± 0.12	2	-0.48 ± 0.09	–
Sc I	-0.49 ± 0.05	3	-0.37 ± 0.05	–
V I	-0.33 ± 0.09	3	-0.02 ± 0.07	–
K I	-0.74 ± 0.12	1	–	–
O I*	-0.41 ± 0.01	118	–	–
Y I	-0.30 ± 0.12	1	–	–
Th I	-0.46 ± 0.04	13	–	–
[M/H]ˆ	-0.49 ± 0.04	–	–	–
[α/M]†	-0.01 ± 0.08	–	–	–

NOTE—*The oxygen abundance is inferred from OH lines.
ˆAverage abundance of all elements.
†Average abundance of Mg I, Si I, Ti I, O I and Ca I alpha elements.

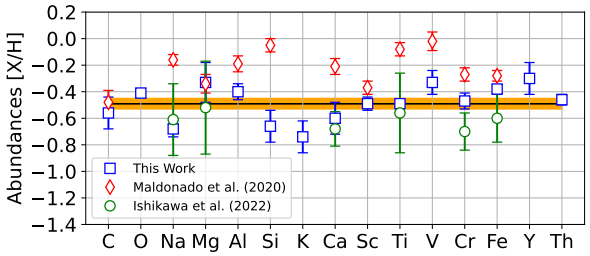

Figure 12. The chemical abundance of 15 different elements are determined via χ^2 spectral fitting of our data using the PHOENIX-ACES synthetic spectra. The blue squares represent the solar-normalized [X/H] abundance of each element. The solid black line and its orange shade represent the overall metallicity and its corresponding uncertainty. The red diamonds and green circles represent the abundances from Maldonado et al. (2020) and Ishikawa et al. (2022), respectively.

is indirectly inferred from the OH absorption lines (see Figure 11).

The [α/M] value determined in this work is -0.01 ± 0.08 dex, which is lower than the typical 0.2 ± 0.1 dex alpha abundance of metal-poor F and G stars in the thick disk (e.g. Bensby et al. 2014). However, recent observations from the APOGEE DR16 database (see Figure 13, Majewski et al. 2016; Ahumada et al. 2020) indicate that the trend of super solar alpha abundance in metal-poor stars may not be as pronounced for M dwarfs. Many M dwarfs in the APOGEE dataset, with metallicities similar to Barnard's star, show [α/M] values around 0 dex. This deviation is also observed by Ishikawa et al. 2022, where their Figure 13 distinctly illustrates that individual alpha elements vs metallicity in some M dwarfs are considerably lower than what is typically observed in thick disk FGK stars.

5. DISCUSSION

Our analysis, based on the use of several groups of lines to determine the effective temperature, has yielded a $T_{\rm eff} = 3231 \pm 21$ K for Barnard's star, consistent with the value of 3238 ± 11 K inferred from the interferometric method (Mann et al. 2013), which is the most fundamental method for $T_{\rm eff}$ determination but is more observationally expensive than spectroscopy.

As shown in Figure 14, our $T_{\rm eff}$ and [M/H] estimates show a fair agreement with most of previous works based on high-resolution spectroscopy but some significant variations are observed. Indeed, it is interesting

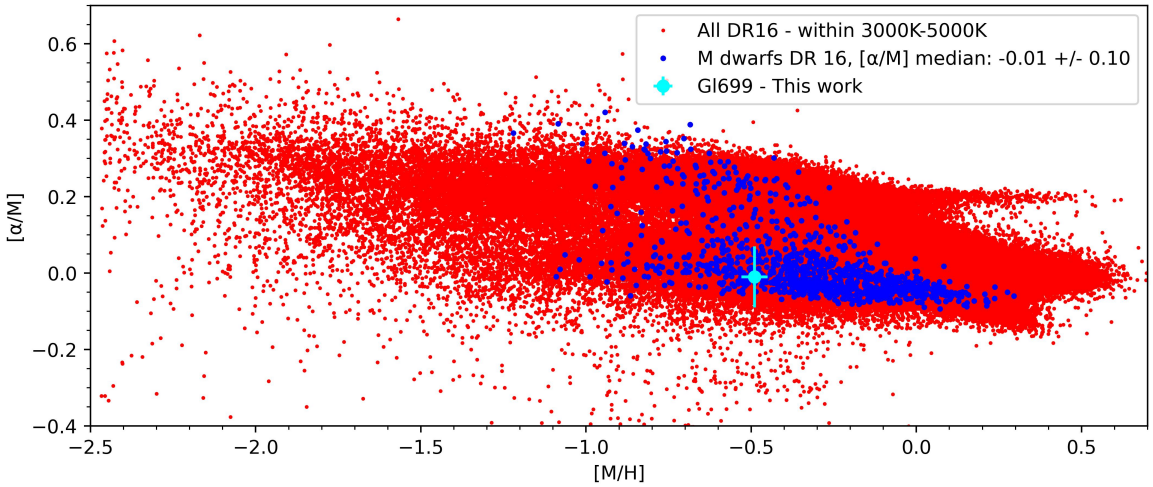

Figure 13. [α/M] vs [M/H] from APOGEE DR16 for all different types of stars within $T_{\rm eff}$ range of 3000 K to 5000 K (red circles) and M dwarfs (blue circles). The [α/M] of Barnard's star from this work is highlighted with a cyan circle. While an anti-correlation is evident in the plot, not all M dwarfs have followed the same trend strictly.

to note the $T_{\rm eff}$ and [M/H] values inferred from this work differ significantly from Cristofari et al. (2022a) even though both these analyses are based on the same SPIRou dataset. In Cristofari et al. (2022a), four different $T_{\rm eff}$ and metallicity values were presented, assuming various scenarios (e.g. fixed and variable $\log g$ for PHOENIX and MARCS models), showing significant discrepancies due to the choice of synthetic models and line lists, leading to different results for the stellar parameters (the reported value in Figure 14 is for the case of fixed $\log g$ with PHOENIX models that is similar to our analysis). Furthermore, Fouqué et al. (2018) adopted a different approach by relying on equivalent-width measurements on ESPaDOnS spectra. These apparent discrepancies are likely related to the choice of different wavelength regimes and systematic effects resulting from a mismatch between observations and models, as shown in this work. As illustrated in Figure 8, not only does using the molecular features of Y and J bands (e.g., FeH) increase the probability of overestimating the $T_{\rm eff}$, but different choices of metallicity and $T_{\rm eff}$ can also interchangeably over- or under-estimate these parameters depending on the lines' wavelength regime. The effect of synthetic caveats varies depending on which part of the spectrum is used for the analysis, consequently impacting the determined fundamental parameters. Due to the group-fitting nature of our method, our work's estimated $T_{\rm eff}$ is less sensitive to the choice of spectral feature; this methodology provides a mean of calibrating other inherent uncertainties associated with a given choice of synthetic models.

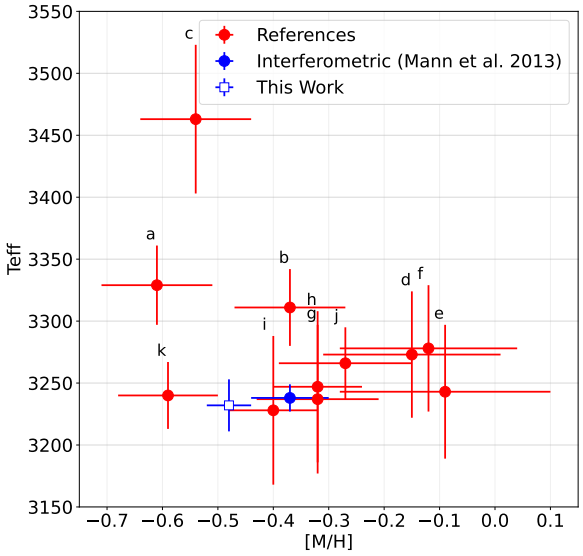

Figure 14. $T_{\rm eff}$ and Metallicity of Barnard's star from different spectroscopic works. References: a. Cristofari et al. (2022a) b. Cristofari et al. (2022b) c. Fouqué et al. (2018) d. Schweitzer et al. (2019) e. Passegger et al. (2020) f. Passegger et al. (2018) g. Gaidos et al. (2014) h. Gaidos & Mann (2014) i. Mann et al. (2015) j. Rojas-Ayala et al. (2012) k. Marfil et al. (2021)

By fixing the $T_{\rm eff}$ and $\log g$ in the models, we determined the chemical abundances of 15 different elements through χ^2 fitting of 210 individual atomic lines or molecular bands. Figure 12 and Table 3 provide a comparison of our abundance measurements with that

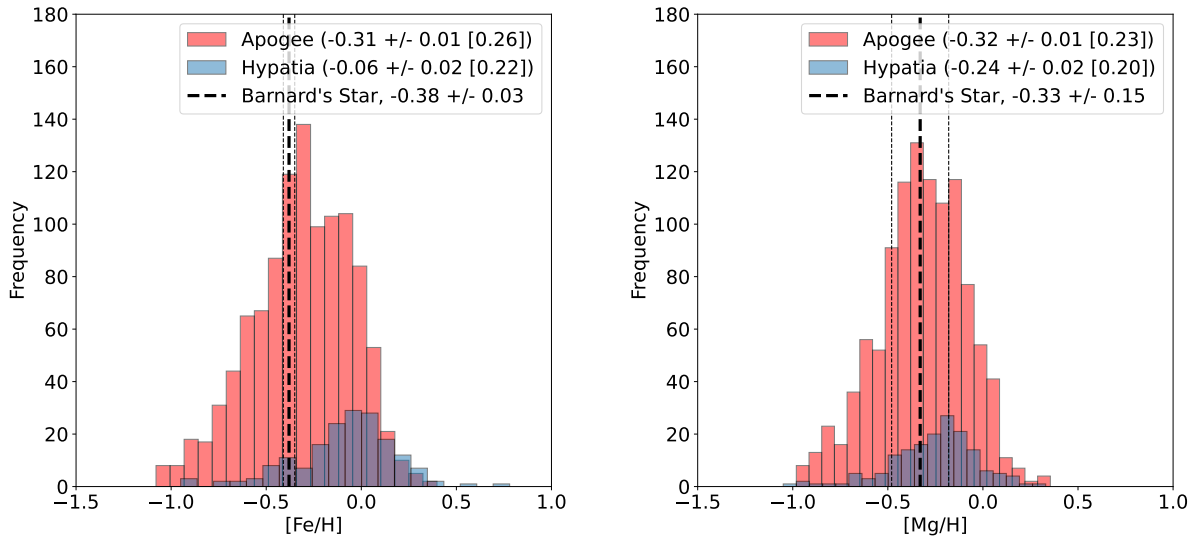

Figure 15. Comparison between the chemistry of M dwarfs from the APOGEE database (DR16) and Hypatia Catalog. The vertical dashed lines show Barnard's star's abundances from this work and their uncertainties. *Left panel:* The [Fe/H] distribution of M dwarfs from both databases. Barnard's star's [Fe/H] from this work (the black vertical dashed line) is consistent with the APOGEE database but there is a noticeable tendency toward solar metallicity in the Hypatia Catalog. *Right panel:* The [Mg/H] distribution of M dwarfs from both databases. The solar tendency in the Hypatia catalog is less severe for the Mg distribution, yet our result is still more consistent with the APOGEE abundances. The legend represents the mean ± relative uncertainty [standard deviation] for each database.

from the literature based on high-resolution spectroscopic observations. Ishikawa et al. (2022) used the high-resolution spectra from the IRD/Subaru Telescope, with their data covering a wide wavelength range from 0.97-1.75μm (Y, J, and H bands), comparable to parts of the SPIRou wavelength range. They determined the chemical abundances of several M dwarfs, including Barnard's star, by comparing the equivalent width of tens of spectral features with those of MARCS synthetic models. Maldonado et al. (2020) developed a novel method to determine stellar abundances in M dwarfs using high-resolution optical spectra. They trained their model, which uses principal component analysis and sparse Bayesian methods, on M dwarfs orbiting FGK primaries. This model was then applied to a large sample of M dwarfs, including Barnard's star.

Our results are consistent with abundance measurements from Ishikawa et al. (2022) with respect to the large uncertainties of their studies. Note that the adopted $T_{\rm eff}$ and $\log g$ in Ishikawa et al. (2022) are 3259 ± 157 K and 5.076 ± 0.028 dex, that are similar to our adopted value. This implies that a change in $T_{\rm eff}$ alone would not have put these into better agreement. Our abundance measurements of Fe, Mg, C and Sc are within 2σ of those of Maldonado et al. (2020), but others, most notably Na and Si, are higher than our abundances. This comparison emphasizes the difficulty of inferring accurate abundance measurements of individual elements from high-resolution spectroscopy. It is difficult to identify the cause for such discrepancies but the use of the different synthetic models, in addition to the choice of lines, are likely the primary reasons.

5.1. *Fe, C, Si, Mg and O*

Several studies have unveiled a correlation between the metallicty of extrasolar host stars and the occurence rate of gas giant exoplanets (Fischer & Valenti 2005; Bond et al. 2006; Guillot et al. 2006). Specifically, these works have revealed that host stars are typically enriched in Fe, C, Si, Mg, and Al at various levels. These elements are the building blocks of planetary cores that lead to the formation of both rocky and giant planets. Since there is both empirical and theoretical evidence that stellar relative abundances of refractory elements are a good proxy for planets (Dorn et al. 2017), one can get some constraints on the chemical composition of planetary cores through stellar abundance measurements. The near-infrared spectrum provides several spectral lines for abundance measurements of refractory elements (i.e. Fe, Si, Mg) as well as for C and O. The C/O ratio in the atmosphere of gas giant exoplanets provides some constraint on the planet formation location within the circumstellar disk (Öberg et al. 2011).

Table 4. Abundance ratios for Barnard's star

X/H	This Work	Sun†	APOGEE*	Hypatia*
C/O	0.39 ± 0.32	0.55 ± 0.17	[0.25, 0.76]	–
Mg/Si	2.63 ± 0.52	1.23 ± 0.12	[0.87, 2.20]	[0.32, 1.83]
Fe/Mg	0.71 ± 0.42	0.79 ± 0.14	[0.38, 1.26]	[0.42, 2.22]
Fe/O	0.07 ± 0.08	0.07 ± 0.16	[0.03, 0.09]	–

NOTE— † Photospheric abundance ratios from Asplund et al. (2009).
*95% confidence interval of the M dwarf population (∼1000) from APOGEE DR16 (Majewski et al. 2016; Ahumada et al. 2020) and (∼140) Hypatia database (Hinkel et al. 2014).

Table 4 gives the C/O, Mg/Si, Fe/Mg, and Fe/O ratios of Barnard's star compared to that of M dwarfs from the APOGEE database[5] (DR16, Majewski et al. 2016, Ahumada et al. 2020) and the Hypatia Catalog (Hinkel et al. 2014). While Mg/Si is noticeably larger than the solar value, all ratios are within the 95% confidence interval of the M dwarf population, with respect to their uncertainties.

It is also interesting to note that there are significant differences in the [Mg/H] and [Fe/H] distributions from APOGEE and Hypathia (see Figure 15), highlighting the fact that abundance measurements in the literature suffer from fairly large dispersion and, likely, significant systematic uncertainties due to different methodology. For instance, the APOGEE database is derived from homogeneous measurements from the same instrument using a common analysis methodology while the Hypathia catalog is a collection of heterogeneous abundance measurements from various sources in the literature.

5.1.1. *Contamination of Si I Lines*

By altering the $T_{\rm eff}$ of a star, the depth and equivalent width of its spectral lines change nonlinearly at varying rates, depending on the nature of the spectral features. In most cases, molecular bands can either entirely suppress or contaminate the atomic wings or nearby weaker lines. This sensitivity is particularly significant for absorption lines that are inherently weak within the spectrum. Silicon lines serve as prime examples, illustrating the importance of considering temperature sensitivity in chemical spectroscopy. As an example, for a star with metallicity comparable to Barnard's star, a $T_{\rm eff}$ of 3600 K represents a threshold for precisely measuring the abundance of the commonly used Si I at 1589.27 nm (see Figure 16). Moreover, for spectra with a medium spectral resolution below 25000 (e.g., that of the APOGEE database), this specific Si line may fully or partially merge with its adjacent OH line, leading to a wrong estimation of the overall Si abundance.

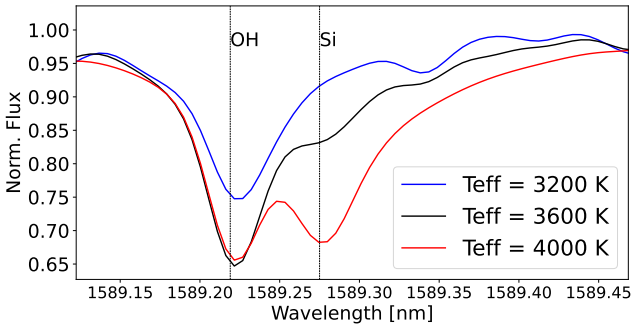

Figure 16. Comparison between three synthetic spectra from the PHOENIX-ACES model convolved to the resolution of SPIRou, with the same metallicity of −0.5 dex but different effective temperatures. This Si I line completely dissolves in the OH molecular line for temperatures lower than 3500 K.

To more effectively demonstrate the impact of temperature sensitivity on the chemical abundances of weak lines, we used the APOGEE database (Majewski 2016) to investigate the chemical behavior of M dwarfs at various temperatures and to identify any potential inconsistencies between the chemistry of our target and similar M dwarfs in the APOGEE database. This allows us to closely examine the Si abundance of M dwarfs with different effective temperatures.

Generally, no relationship is expected between an element's chemical abundance and a star's effective temperature. However, upon examining the chemical abun-

[5] The APOGEE database is an IR spectroscopic survey comprising hundreds of thousands of stars spanning the entire Galactic bulge, bar, disk, and halo. This survey covers the wavelength range of 1.5-1.7μm in the H band, with a spectral resolution R=22500 (Gunn et al. 2006). This database provides estimates for stellar parameters and abundances of various elements.

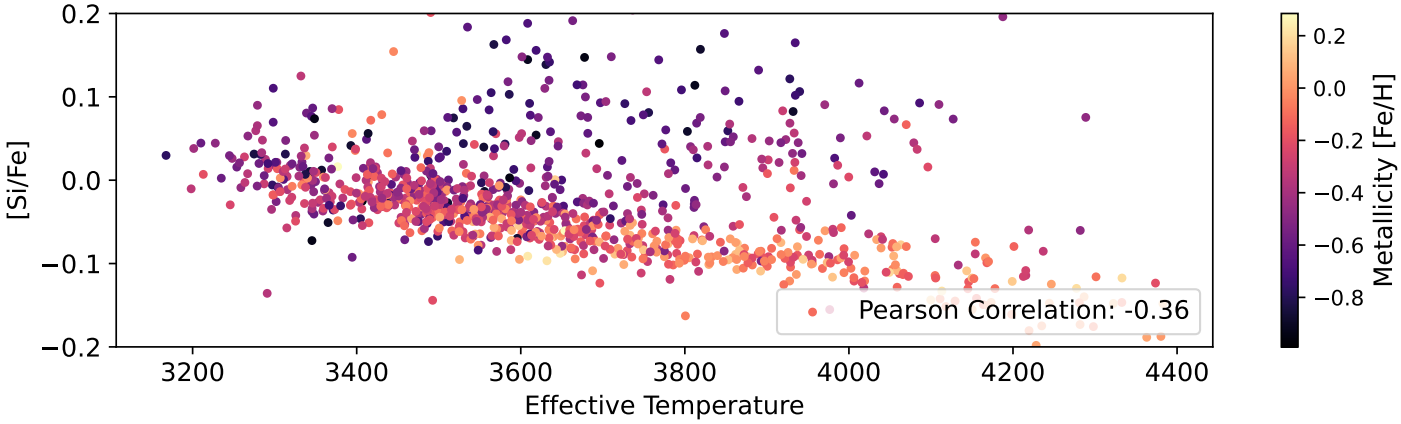

Figure 17. The silicon abundance of APOGEE M dwarfs with $\log g$ range of 4.0 to 6.0 dex, and effective temperature range of 3100 K to 4000 K. There is an unexpected anti-correlation between the silicon abundance and $T_{\rm eff}$.

dances of M dwarfs from the APOGEE DR16, a distinct anti-correlation is apparent in the [Si/Fe] distribution as a function of temperature (see Figure 17). This overestimation of Si abundance is more significant in colder and/or metal-poorer stars. This anti-correlation is likely due to the contamination of nearby strong lines on Si abundance measurements. For cooler stars, the OH lines fully dominate the adjacent weaker lines, while for hotter, metal-poor stars, the depth of the Si line becomes extremely weak, leading to a similar effect of merging with nearby lines. In either case, an overestimation of abundance is a probable outcome. We examined the existence of such an anti-correlation for other elements and discovered none or only minor comparable trends for the remaining elements. The conclusion from this exercise is that the Si abundance reported in APOGEE should be taken with caution specially for late M dwarfs.

6. SUMMARY

Systematic caveats in synthetic models can significantly impact the chemical spectroscopy of stars. This work has highlighted some of the critical caveats that can lead to mis-estimation of fundamental stellar parameters, such as $T_{\rm eff}$, and different chemical abundances for Barnard's star.

We examined the high-resolution spectrum of Barnard's star from the SPIRou instrument via a χ^2 analysis of multiple absorption lines using the PHOENIX-ACES synthetic spectra. We determined the effective temperature, overall metallicity and chemical abundances of 15 different elements. For the effective temperature, we employed a novel method based on the simultaneous group fitting of numerous spectral features, ascertaining the $T_{\rm eff}$ by examining the sensitivity of these spectral features as a function of wavelength.

To minimize the effects of uncertainties associated with synthetic models, we developed a pipeline that identifies common spectral features between observed spectra and synthetic models that are at least 5% deep from the continuum level and are not saturated. Using the cleaned set of spectral features, we introduced a new method for determining $T_{\rm eff}$. The heart of this method involves group fitting of hundreds of well-selected spectral features that are not affected by various caveats (continuum mismatch and other inconsistencies between observations and models), as a function of wavelength. Through this method, we determined $T_{\rm eff}$ for different fixed metallicities, and found the optimal $T_{\rm eff}$ with the lowest variation across different wavelengths. We determined $T_{\rm eff} = 3231 \pm 21$ K for Barnard's star, consistent with the interferometric value of 3238 ± 11 K, which is the most reliable method for $T_{\rm eff}$ determination. Additionally, we showed how previous spectroscopic works might have under- or over-estimated $T_{\rm eff}$, possibly due to not considering the various caveats discussed in this work.

Next, using the determined $T_{\rm eff}$ and fixing $\log g$ from the literature, and utilizing the NIST and BT-Settl PHOENIX line lists, we measured the chemical abundances of 15 different elements. This includes the chemical abundances of Mg, C, Si, and Fe, which play a significant role in exoplanet interior modeling studies. We compared our results with the abundances determined in recent independent literature. Our results were consistent with Ishikawa et al. (2022) and partially consistent with Maldonado et al. (2020), emphasizing the importance of line selection and methodology in detailed chemical spectroscopy of M dwarfs.

This work emphasizes the need to improve atmosphere models (at least the PHOENIX models used in this work) as there are significant discrepancies between the observations and models. Only a few hundred lines were effectively used in our analysis as a result while several thousands could be used should there be a better agree-

ment between observations and synthetic modes. This detailed and comprehensive analysis should be repeated for other set of models such as MARCS (Gustafsson et al. 2008) and SPHINX (Iyer et al. 2023). The high quality NIR spectrum of Barnard's star (broad wavelength coverage, very high SNR and excellent telluric correction) presented here is an ideal data set for such detailed investigations. The full potential of NIR chemical spectroscopy has yet to be harnessed with the development of better atmosphere models.

ACKNOWLEDGMENTS

We would like to thank the anonymous referee for the constructive comments and thorough review of this manuscript.

This work is based on observations obtained at the Canada-France-Hawaii Telescope (CFHT) which is operated from the summit of Maunakea by the National Research Council of Canada, the Institut National des Sciences de l'Univers of the Centre National de la Recherche Scientifique of France, and the University of Hawaii. The observations at the Canada-France-Hawaii Telescope were performed with care and respect from the summit of Maunakea which is a significant cultural and historic site.

In this work, we extend our heartfelt gratitude and pay tribute to the late France Allard, whose significant contributions to astrophysics and her instrumental role in the field of synthetic modeling have been invaluable to our research. Throughout this paper, we heavily relied on her pioneering synthetic models, which provided the essential foundation for our analysis and findings. France Allard's groundbreaking work has left a lasting impact on the scientific community, and her legacy continues to inspire current and future generations of researchers.

This work is partly funded through the National Science and Engineering Research Council of Canada through the Discovery Grant program and the CREATE training program on New Technologies for Canadian Observatories. We also acknowledge the generous financial support of the Trottier Family Foundation for Trottier Institute for Research on Exoplanets.

We acknowledge funding from the French ANR under contract number ANR18CE310019 (SPlaSH). This work is supported in part by the French National Research Agency in the framework of the Investissements d'Avenir program (ANR-15-IDEX-02), through the funding of the "Origin of Life" project of the Grenoble-Alpes University.

JFD acknowledges funding from the European Research Council (ERC) under the H2020 research & innovation program (grant agreement #740651 NewWorlds)

E.M. acknowledges funding from FAPEMIG under project number APQ-02493-22 and research productivity grant number 309829/2022-4 awarded by the CNPq, Brazil.

The research shown here acknowledges use of the Hypatia Catalog Database, an online compilation of stellar abundance data as described in Hinkel et al. (2014), which was supported by NASA's Nexus for Exoplanet System Science (NExSS) research coordination network and the Vanderbilt Initiative in Data-Intensive Astrophysics (VIDA).

Facilities: CFHT/SPIRou

Software: `Astropy` (Astropy Collaboration et al. 2018); `matplotlib` (Hunter 2007); `SciPy` (Virtanen et al. 2020); `NumPy` (Harris et al. 2020) .

REFERENCES

Ahumada, R., Prieto, C. A., Almeida, A., et al. 2020, ApJS, 249, 3, doi: 10.3847/1538-4365/ab929e

Allard, F., & Hauschildt, P. H. 1996, arXiv preprint astro-ph/9601150

Allard, F., Homeier, D., & Freytag, B. 2010, arXiv preprint arXiv:1011.5405

Allard, F., Homeier, D., & Freytag, B. 2012, Philosophical Transactions of the Royal Society of London Series A, 370, 2765, doi: 10.1098/rsta.2011.0269

Allard, N., Allard, F., Hauschildt, P., Kielkopf, J., & Machin, L. 2003, Astronomy & Astrophysics, 411, L473

Artigau, É., Malo, L., Doyon, R., et al. 2018, The Astronomical Journal, 155, 198

Asplund, M., Grevesse, N., Sauval, A. J., & Scott, P. 2009, Annual review of astronomy and astrophysics, 47

Astropy Collaboration, Price-Whelan, A. M., Sipőcz, B. M., et al. 2018, AJ, 156, 123, doi: 10.3847/1538-3881/aabc4f

Bensby, T., Feltzing, S., & Oey, M. 2014, Astronomy & Astrophysics, 562, A71

Blanco-Cuaresma, S. 2019, Monthly Notices of the Royal Astronomical Society, 486, 2075

Blanco-Cuaresma, S., Soubiran, C., Heiter, U., & Jofré, P. 2014, Astronomy & Astrophysics, 569, A111

Bond, J., Tinney, C., Butler, R. P., et al. 2006, Monthly Notices of the Royal Astronomical Society, 370, 163

Bonfils, X., Delfosse, X., Udry, S., et al. 2013, Astronomy & Astrophysics, 549, A109

Boyajian, T. S., Von Braun, K., Van Belle, G., et al. 2012, The Astrophysical Journal, 757, 112

Campbell, B., Walker, G. A., & Yang, S. 1988, The Astrophysical Journal, 331, 902

Casagrande, L., Flynn, C., & Bessell, M. 2008, Monthly Notices of the Royal Astronomical Society, 389, 585

Chabrier, G., & Baraffe, I. 2000, Annual Review of Astronomy and Astrophysics, 38, 337

Cloutier, R., & Menou, K. 2020, AJ, 159, 211, doi: 10.3847/1538-3881/ab8237

Cook, N. J., Artigau, É., Doyon, R., et al. 2022, Publications of the Astronomical Society of the Pacific, 134, 114509

Cristofari, P., Donati, J., Masseron, T., et al. 2022a, Monthly Notices of the Royal Astronomical Society, 511, 1893

—. 2022b, Monthly Notices of the Royal Astronomical Society, 516, 3802

Donati, J., Kouach, D., Moutou, C., et al. 2020, Monthly Notices of the Royal Astronomical Society, 498, 5684

Dorn, C., Hinkel, N. R., & Venturini, J. 2017, A&A, 597, A38, doi: 10.1051/0004-6361/201628749

Dressing, C. D., & Charbonneau, D. 2015, The Astrophysical Journal, 807, 45

Fischer, D. A., & Valenti, J. 2005, The Astrophysical Journal, 622, 1102

Fouqué, P., Moutou, C., Malo, L., et al. 2018, Monthly Notices of the Royal Astronomical Society, 475, 1960

Gaidos, E., & Mann, A. W. 2014, The Astrophysical Journal, 791, 54

Gaidos, E., Mann, A. W., Kraus, A., & Ireland, M. 2016, Monthly Notices of the Royal Astronomical Society, 457, 2877

Gaidos, E., Mann, A., Lépine, S., et al. 2014, Monthly Notices of the Royal Astronomical Society, 443, 2561

Guillot, T., Santos, N. C., Pont, F., et al. 2006, Astronomy & Astrophysics, 453, L21

Gunn, J. E., Siegmund, W. A., Mannery, E. J., et al. 2006, The Astronomical Journal, 131, 2332

Gustafsson, B., Edvardsson, B., Eriksson, K., et al. 2008, Astronomy & Astrophysics, 486, 951

Hargreaves, R. J., Hinkle, K. H., Bauschlicher, C. W., et al. 2010, The Astronomical Journal, 140, 919

Harris, C. R., Millman, K. J., van der Walt, S. J., et al. 2020, Nature, 585, 357, doi: 10.1038/s41586-020-2649-2

Hauschildt, P. H., Baron, E., & Allard, F. 1997, The Astrophysical Journal, 483, 390

Henry, T. J., Kirkpatrick, J. D., & Simons, D. A. 1994, The Astronomical Journal, 108, 1437

Hinkel, N. R., Timmes, F. X., Young, P. A., Pagano, M. D., & Turnbull, M. C. 2014, AJ, 148, 54, doi: 10.1088/0004-6256/148/3/54

Hojjatpanah, S., Figueira, P., Santos, N., et al. 2019, Astronomy & Astrophysics, 629, A80

Hsu, D. C., Ford, E. B., & Terrien, R. 2020, MNRAS, 498, 2249, doi: 10.1093/mnras/staa2391

Hunter, J. D. 2007, Computing in Science and Engineering, 9, 90, doi: 10.1109/MCSE.2007.55

Husser, T. O., Wende-von Berg, S., Dreizler, S., et al. 2013, A&A, 553, A6, doi: 10.1051/0004-6361/201219058

Ishikawa, H. T., Aoki, W., Hirano, T., et al. 2022, The Astronomical Journal, 163, 72

Iyer, A. R., Line, M. R., Muirhead, P. S., Fortney, J. J., & Gharib-Nezhad, E. 2023, The Astrophysical Journal, 944, 41

Lamb, M., Venn, K., Andersen, D., et al. 2016, Monthly Notices of the Royal Astronomical Society, stw2865

Latham, D. W., Mazeh, T., Stefanik, R. P., Mayor, M., & Burki, G. 1989, Nature, 339, 38

Lim, O., Benneke, B., Doyon, R., et al. 2023, The Astrophysical Journal Letters, 955, L22

Majewski, S. 2016, Astronomische Nachrichten, 337, 863
Majewski, S. R., APOGEE Team, & APOGEE-2 Team. 2016, Astronomische Nachrichten, 337, 863, doi: 10.1002/asna.201612387
Maldonado, J., Micela, G., Baratella, M., et al. 2020, Astronomy & Astrophysics, 644, A68
Mann, A. W., Feiden, G. A., Gaidos, E., Boyajian, T., & von Braun, K. 2015, The Astrophysical Journal, 804, 64
Mann, A. W., Gaidos, E., & Ansdell, M. 2013, The Astrophysical Journal, 779, 188
Marfil, E., Tabernero, H. M., Montes, D., et al. 2021, arXiv preprint arXiv:2110.07329
Martinez, A. O., Crossfield, I. J., Schlieder, J. E., et al. 2017, The Astrophysical Journal, 837, 72
Mayor, M., & Queloz, D. 1995, nature, 378, 355
Muirhead, P. S., Becker, J., Feiden, G. A., et al. 2014, The Astrophysical Journal Supplement Series, 213, 5
Mulders, G. D., Pascucci, I., & Apai, D. 2015, The Astrophysical Journal, 814, 130
NIST. 2019, Atomic Spectra Database, [Data file]. Available from https://www.nist.gov/pml/atomic-spectra-database
Öberg, K. I., Murray-Clay, R., & Bergin, E. A. 2011, ApJL, 743, L16, doi: 10.1088/2041-8205/743/1/L16
Önehag, A., Heiter, U., Gustafsson, B., et al. 2012, Astronomy & Astrophysics, 542, A33
Passegger, V., Reiners, A., Jeffers, S., et al. 2018, Astronomy & Astrophysics, 615, A6
Passegger, V., Schweitzer, A., Shulyak, D., et al. 2020, Astronomy & Astrophysics, 634, C2
Passegger, V., Bello-García, A., Ordieres-Meré, J., et al. 2021, arXiv preprint arXiv:2111.14950
Rajpurohit, A., Allard, F., Rajpurohit, S., et al. 2018, Astronomy & Astrophysics, 620, A180
Reiners, A., Zechmeister, M., Caballero, J., et al. 2018, Astronomy & Astrophysics, 612, A49
Reylé, C., Jardine, K., Fouqué, P., et al. 2021, A&A, 650, A201, doi: 10.1051/0004-6361/202140985
Rojas-Ayala, B., Covey, K. R., Muirhead, P. S., & Lloyd, J. P. 2010, The Astrophysical Journal Letters, 720, L113
—. 2012, The Astrophysical Journal, 748, 93
Schweitzer, A., Passegger, V., Cifuentes, C., et al. 2019, Astronomy & Astrophysics, 625, A68
Skrutskie, M., Cutri, R., Stiening, R., et al. 2006, The Astronomical Journal, 131, 1163
Souto, D., Cunha, K., García-Hernández, D., et al. 2017, The Astrophysical Journal, 835, 239
Souto, D., Cunha, K., Smith, V. V., et al. 2020, arXiv preprint arXiv:2001.05597
Stassun, K. G., Oelkers, R. J., Paegert, M., et al. 2019, The Astronomical Journal, 158, 138
Takeda, Y., Ohkubo, M., & Sadakane, K. 2002, Publications of the Astronomical Society of Japan, 54, 451
Tannock, M. E., Metchev, S., Hood, C. E., et al. 2022, Monthly Notices of the Royal Astronomical Society, 514, 3160
Toledo-Padrón, B., González Hernández, J. I., Rodríguez-López, C., et al. 2019, Monthly Notices of the Royal Astronomical Society, 488, 5145
Vallenari, A., Prusti, T., de Bruijne, J., et al. 2021, Astronomy and Astrophysics-A&A, 649, A1
Veyette, M. J., Muirhead, P. S., Mann, A. W., & Allard, F. 2016, The Astrophysical Journal, 828, 95
Virtanen, P., Gommers, R., Oliphant, T. E., et al. 2020, Nature Methods, 17, 261, doi: 10.1038/s41592-019-0686-2
Wenger, M., Ochsenbein, F., Egret, D., et al. 2000, Astronomy and Astrophysics Supplement Series, 143, 9
Winters, J. G., Henry, T. J., Jao, W.-C., et al. 2019, The Astronomical Journal, 157, 216
Zacharias, N., Finch, C., Girard, T., et al. 2013, The Astronomical Journal, 145, 44

APPENDIX

A. SPECTROSCOPIC DATA AND ABUNDANCES OF ATOMIC LINES

This appendix comprises two tables. Table A.1 presents spectroscopic data (e.g., wavelength and normalized flux) of Barnard's star and a synthetic model with a $T_{\rm eff}$ of 3200 K, [M/H] of −0.5, and $\log g$ of 5 dex. Table A.2 details abundance values for various elemental lines used in this study. We compiled this elemental list from NIST database (NIST 2019) and PHOENIX BT-Settl (Allard et al. 2010) line list. In Table A.2, the column labeled "Nearby Lines" identifies the presence of nearby spectral feature based on our line lists. It is important to note that while these nearby lines indicate the proximity of other lines to our target lines, it remains unclear to what extent, if any, these nearby lines influence the strength of the target lines. Due to the inability to individually resolve these lines and their unknown true relative strength, their impact is difficult to quantify. However as a test we have empirically determined that there are no significant abundance differences using either the whole list vs the ones without the potentially contaminated ones (see Figure A.1). Also note that the "Error" columns represents the standard deviation of all 50 MC measurements for a single line. When the value in this column is zero, it indicates that the noise in the spectrum was too subtle to affect the abundances, suggesting that the systematic uncertainty for the line was below the grid's 0.1 dex metallicity sensitivity.

Table A.1. Spectroscopic Data of Barnard's star and a similar synthetic model

Wavelength (vacuum, nm)	Data Flux	Error	Model Flux
970.000	0.995	0.001	0.995
970.003	0.998	0.001	0.998
970.007	1.001	0.001	1.002
970.010	0.999	0.001	1.005
970.013	1.001	0.001	1.007
970.017	0.999	0.001	1.008
970.020	0.997	0.001	1.008
970.023	0.996	0.001	1.008
970.026	0.995	0.001	1.006
970.030	0.997	0.001	1.002
...	...	...	...

NOTE—Table A.1 is published in its entirety in machine-readable format.

The synthetic model used for comparison has a $T_{\rm eff}$ of 3200 K, [M/H] of −0.5, and $\log g$ of 5 dex.

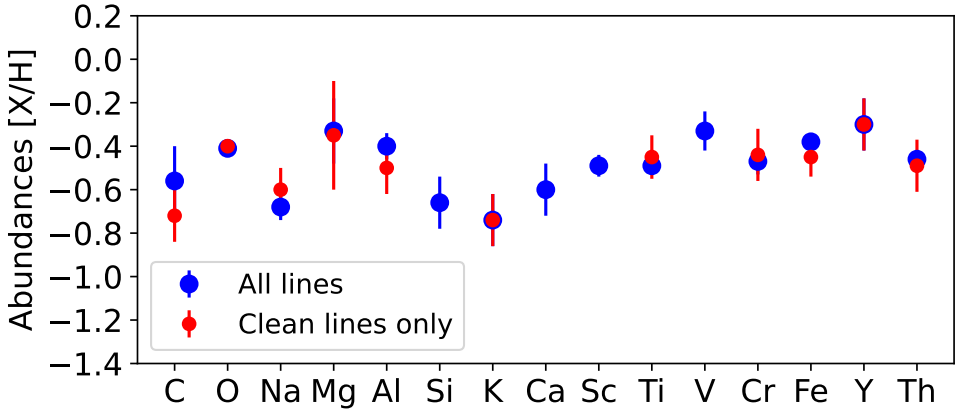

Figure A.1. There are no significant abundance differences using either the whole list vs the ones without the potentially contaminated ones and both cases are consistent within their uncertainties.

Table A.2. Characteristics of elemental spectral lines

Element	Central Wavelength (vacuum, nm)	[X/H] (dex)	Error (dex)	Line Depth	Ref	Nearby Lines
Fe I	1122.396	−0.19	0.040	0.05	NIST	—
Fe I	1130.195	−0.65	0.050	0.16	Ph-BT	—
Fe I	1288.329	−0.30	0.020	0.16	Ph-BT	—
Fe I	1400.831	−0.40	0.000	0.24	NIST	OH
Fe I	1467.038	−0.40	0.010	0.17	NIST	OH
Fe I	1538.831	−0.10	0.000	0.13	NIST	OH
Fe I	1543.184	−0.40	0.038	0.21	NIST	OH
Fe I	1578.104	−0.50	0.000	0.22	NIST	OH
Fe I	1590.200	−0.49	0.027	0.28	NIST	OH
Fe I	1591.714	−0.30	0.000	0.27	NIST	OH, Mg, Cr
Fe I	1604.710	−0.49	0.035	0.07	NIST	—
Fe I	1607.403	−0.60	0.000	0.26	NIST	OH
Fe I	1619.475	−0.41	0.027	0.29	NIST	OH
Fe I	1623.006	−0.30	0.000	0.13	NIST	OH
Fe I	1623.609	−0.44	0.048	0.11	NIST	OH
Fe I	1634.160	−0.40	0.000	0.08	NIST	OH
Fe I	1661.217	−0.20	0.000	0.22	NIST	OH
Fe I	1672.364	−0.50	0.000	0.30	NIST	Al, OH
Fe I	1675.373	−0.40	0.000	0.20	NIST	OH
Fe I	1688.363	−0.40	0.000	0.20	NIST	OH, Th
Fe I	1688.941	−0.30	0.000	0.18	NIST	OH
Fe I	1689.980	−0.40	0.000	0.23	NIST	OH
Fe I	1690.350	−0.30	0.000	0.25	NIST	OH
Fe I	1705.684	−0.20	0.000	0.20	NIST	OH
Fe I	1733.882	−0.30	0.000	0.17	NIST	OH
Fe I	2179.433	−0.19	0.027	0.10	NIST	H_2O
Fe I	2294.137	−0.70	0.000	0.20	NIST	CO
Fe I	2323.967	−0.60	0.000	0.17	NIST	—
Fe I	2387.064	−0.30	0.000	0.29	NIST	H_2O
Mg I	1488.160	−0.10	0.000	0.16	Ph-BT	—
Mg I	1591.718	−0.30	0.000	0.27	NIST	OH, Fe, Cr

Table A.2. Characteristics of elemental spectral lines

Element	Central Wavelength (vacuum, nm)	[X/H] (dex)	Error (dex)	Line Depth	Ref	Nearby Lines
Mg I	1711.330	−0.60	0.050	0.17	Ph-BT	—
Ti I	1178.378	−0.63	0.045	0.16	Ph-BT	—
Ti I	1260.371	−0.70	0.000	0.14	Ph-BT	H_2O
Ti I	1267.458	−0.58	0.039	0.15	Ph-BT	—
Ti I	1274.840	−0.60	0.000	0.05	Ph-BT	H_2O, Cr
Ti I	1281.499	−0.33	0.056	0.12	Ph-BT	—
Ti I	1292.342	−0.60	0.050	0.08	Ph-BT	—
Ti I	1397.680	−0.50	0.000	0.22	NIST	OH
Ti I	1466.894	−0.11	0.070	0.06	NIST	—
Ti I	1565.798	−0.40	0.000	0.25	NIST	OH
Ti I	1573.491	−0.59	0.032	0.27	NIST	OH
Ti I	1606.950	−0.49	0.031	0.26	NIST	OH
Ti I	1635.652	−0.40	0.000	0.26	NIST	OH
Ti I	1661.012	−0.40	0.000	0.19	NIST	OH
Ti I	1993.948	−0.60	0.001	0.26	NIST	H_2O, Ca
Ti I	2223.892	−0.50	0.000	0.18	Ph-BT	H_2O
Ti I	2324.308	−0.60	0.000	0.16	NIST	CO
Ti I	2328.639	−0.40	0.000	0.13	NIST	CO, Sc
Ti I	2428.846	−0.30	0.000	0.14	Ph-BT	H_2O
Cr I	1147.610	−0.18	0.022	0.14	Ph-BT	V, H_2O
Cr I	1148.770	−0.44	0.048	0.17	Ph-BT	—
Cr I	1161.369	−0.60	0.000	0.22	Ph-BT	TiO, H_2O
Cr I	1253.620	−0.57	0.022	0.07	Ph-BT	TiO
Cr I	1274.844	−0.60	0.000	0.05	NIST	H_2O, Ti
Cr I	1294.060	−0.47	0.022	0.07	Ph-BT	TiO
Cr I	1320.475	−0.60	0.000	0.07	Ph-BT	H_2O
Cr I	1591.731	−0.30	0.000	0.27	NIST	OH, Mg, Fe
Na I	1083.787	−0.50	0.010	0.16	NIST	—
Na I	1268.265	−0.70	0.000	0.29	NIST	H_2O, TiO
Na I	2206.248	−0.80	0.000	0.40	NIST	H_2O
Na I	2338.555	−0.70	0.000	0.26	NIST	—
Ca I	1281.957	−0.60	0.000	0.17	NIST	H_2O
Ca I	1993.914	−0.60	0.001	0.26	NIST	Ti, H_2O
Al I	1125.628	−0.30	0.022	0.22	Ph-BT	V, H_2O
Al I	1125.796	−0.30	0.036	0.27	Ph-BT	Th, TiO
Al I	1672.353	−0.50	0.000	0.30	Ph-BT	Fe, OH
Al I	1675.513	−0.50	0.000	0.27	Ph-BT	—
Si I	1075.231	−0.66	0.010	0.05	Ph-BT	Th
C I	2296.595	−0.72	0.040	0.05	NIST	—
C I	2354.499	−0.40	0.026	0.27	NIST	CO
Sc I	1626.484	−0.57	0.045	0.25	NIST	OH
Sc I	1645.469	−0.50	0.014	0.25	NIST	OH
Sc I	2328.640	−0.40	0.000	0.13	NIST	CO, Ti
V I	1125.610	−0.30	0.022	0.22	Ph-BT	Al
V I	1147.621	−0.18	0.022	0.14	NIST	Cr
V I	2131.777	−0.50	0.043	0.06	NIST	H_2O

Table A.2. Characteristics of elemental spectral lines

Element	Central Wavelength (vacuum, nm)	[X/H] (dex)	Error (dex)	Line Depth	Ref	Nearby Lines
K I	1102.290	−0.74	0.040	0.15	NIST	—
Y I	2399.700	−0.30	0.010	0.21	Ph-BT	—
Th I	1075.237	−0.66	0.010	0.05	Ph-BT	Si
Th I	1125.816	−0.30	0.036	0.27	NIST	Al, TiO
Th I	1391.583	−0.70	0.017	0.09	NIST	OH
Th I	1391.899	−0.35	0.050	0.20	NIST	OH
Th I	1466.534	−0.50	0.000	0.28	NIST	OH
Th I	1557.637	−0.50	0.000	0.29	NIST	OH
Th I	1635.060	−0.27	0.048	0.17	NIST	OH
Th I	1652.792	−0.50	0.000	0.23	NIST	OH
Th I	1673.448	−0.37	0.045	0.16	NIST	OH
Th I	1687.645	−0.40	0.000	0.21	NIST	OH
Th I	1688.391	−0.40	0.000	0.20	NIST	OH, Fe
Th I	1700.934	−0.60	0.022	0.09	NIST	OH
Th I	1710.822	−0.49	0.058	0.08	NIST	—
OH	1391.577	−0.70	0.017	0.09	Ph-BT	Th
OH	1391.888	−0.35	0.050	0.20	Ph-BT	Th
OH	1391.953	−0.40	0.000	0.21	Ph-BT	—
OH	1393.282	−0.38	0.034	0.22	Ph-BT	—
OH	1394.495	−0.40	0.000	0.17	Ph-BT	—
OH	1397.657	−0.50	0.000	0.22	Ph-BT	Ti
OH	1400.822	−0.40	0.000	0.24	Ph-BT	Fe
OH	1405.901	−0.45	0.050	0.23	Ph-BT	—
OH	1408.694	−0.60	0.000	0.19	Ph-BT	—
OH	1413.419	−0.70	0.020	0.15	Ph-BT	—
OH	1416.298	−0.42	0.040	0.20	Ph-BT	—
OH	1418.596	−0.50	0.000	0.16	Ph-BT	—
OH	1434.455	−0.50	0.051	0.24	Ph-BT	—
OH	1456.402	−0.44	0.048	0.26	Ph-BT	—
OH	1461.844	−0.37	0.044	0.15	Ph-BT	—
OH	1466.515	−0.50	0.000	0.28	Ph-BT	Th
OH	1467.031	−0.40	0.010	0.17	Ph-BT	Fe
OH	1469.887	−0.50	0.000	0.21	Ph-BT	—
OH	1476.043	−0.45	0.050	0.06	Ph-BT	—
OH	1477.216	−0.62	0.038	0.21	Ph-BT	—
OH	1483.328	−0.30	0.000	0.15	Ph-BT	—
OH	1500.722	−0.50	0.017	0.26	Ph-BT	—
OH	1505.320	0.10	0.020	0.12	Ph-BT	—
OH	1506.937	−0.10	0.049	0.17	Ph-BT	—
OH	1513.380	−0.30	0.000	0.32	Ph-BT	—
OH	1513.506	−0.52	0.038	0.28	Ph-BT	—
OH	1524.110	−0.45	0.050	0.15	Ph-BT	—
OH	1528.269	−0.50	0.000	0.29	Ph-BT	—
OH	1528.524	−0.50	0.000	0.29	Ph-BT	—
OH	1533.212	−0.30	0.020	0.18	Ph-BT	—
OH	1539.525	−0.41	0.026	0.21	Ph-BT	—

Table A.2. Characteristics of elemental spectral lines

Element	Central Wavelength (vacuum, nm)	[X/H] (dex)	Error (dex)	Line Depth	Ref	Nearby Lines
OH	1539.541	−0.40	0.032	0.21	Ph-BT	—
OH	1540.733	−0.24	0.050	0.15	Ph-BT	—
OH	1542.985	−0.30	0.000	0.12	Ph-BT	—
OH	1543.171	−0.58	0.038	0.21	Ph-BT	Fe
OH	1546.814	−0.17	0.045	0.10	Ph-BT	—
OH	1550.999	−0.50	0.000	0.21	Ph-BT	—
OH	1557.023	−0.30	0.010	0.14	Ph-BT	—
OH	1557.633	−0.50	0.000	0.29	Ph-BT	Th
OH	1559.783	−0.17	0.045	0.08	Ph-BT	—
OH	1563.095	−0.32	0.038	0.28	Ph-BT	—
OH	1563.168	−0.30	0.014	0.25	Ph-BT	—
OH	1565.778	−0.40	0.000	0.25	Ph-BT	Ti
OH	1573.474	−0.59	0.032	0.27	Ph-BT	Ti
OH	1578.115	−0.50	0.000	0.22	Ph-BT	Fe
OH	1583.314	−0.30	0.014	0.13	Ph-BT	—
OH	1583.335	−0.30	0.010	0.13	Ph-BT	—
OH	1590.206	−0.49	0.027	0.28	Ph-BT	Fe
OH	1591.708	−0.30	0.000	0.27	Ph-BT	Mg, Fe, Cr
OH	1604.126	−0.50	0.010	0.24	Ph-BT	—
OH	1604.292	−0.50	0.000	0.24	Ph-BT	—
OH	1606.943	−0.49	0.031	0.26	Ph-BT	Ti
OH	1607.394	−0.60	0.000	0.26	Ph-BT	Fe
OH	1607.984	−0.40	0.017	0.15	Ph-BT	—
OH	1612.829	−0.35	0.050	0.12	Ph-BT	—
OH	1619.454	−0.41	0.027	0.29	Ph-BT	Fe
OH	1621.162	−0.43	0.043	0.25	Ph-BT	—
OH	1622.996	−0.30	0.000	0.13	Ph-BT	—
OH	1623.489	−0.37	0.045	0.13	Ph-BT	—
OH	1623.587	−0.44	0.048	0.11	Ph-BT	Fe
OH	1626.459	−0.57	0.045	0.25	Ph-BT	Sc
OH	1627.024	−0.55	0.050	0.11	Ph-BT	—
OH	1631.692	−0.47	0.044	0.13	Ph-BT	—
OH	1631.736	−0.49	0.045	0.13	Ph-BT	—
OH	1634.149	−0.40	0.000	0.08	Ph-BT	Fe
OH	1635.065	−0.27	0.048	0.17	Ph-BT	Th
OH	1635.196	−0.51	0.034	0.13	Ph-BT	—
OH	1635.670	−0.40	0.000	0.26	Ph-BT	Ti
OH	1636.904	−0.44	0.049	0.26	Ph-BT	—
OH	1645.257	−0.50	0.000	0.23	Ph-BT	—
OH	1645.488	−0.50	0.014	0.25	Ph-BT	Sc
OH	1646.053	−0.50	0.000	0.24	Ph-BT	—
OH	1647.734	−0.40	0.000	0.15	Ph-BT	—
OH	1652.804	−0.50	0.000	0.23	Ph-BT	Th
OH	1653.074	−0.51	0.027	0.24	Ph-BT	—
OH	1653.913	−0.50	0.000	0.25	Ph-BT	—
OH	1658.581	−0.24	0.022	0.17	Ph-BT	—

Table A.2. Characteristics of elemental spectral lines

Element	Central Wavelength (vacuum, nm)	[X/H] (dex)	Error (dex)	Line Depth	Ref	Nearby Lines
OH	1658.686	−0.30	0.010	0.17	Ph-BT	—
OH	1661.000	−0.40	0.000	0.19	Ph-BT	Ti
OH	1661.205	−0.20	0.000	0.22	Ph-BT	Fe
OH	1665.922	−0.55	0.050	0.22	Ph-BT	—
OH	1666.055	−0.60	0.014	0.23	Ph-BT	—
OH	1666.672	−0.50	0.000	0.22	Ph-BT	—
OH	1670.892	−0.50	0.000	0.22	Ph-BT	—
OH	1671.895	−0.52	0.041	0.23	Ph-BT	—
OH	1672.342	−0.50	0.000	0.30	Ph-BT	Al, Fe
OH	1673.435	−0.37	0.045	0.16	Ph-BT	Th
OH	1675.385	−0.40	0.000	0.20	Ph-BT	Fe
OH	1675.630	−0.60	0.010	0.19	Ph-BT	—
OH	1687.651	−0.40	0.000	0.21	Ph-BT	Th
OH	1687.691	−0.50	0.010	0.22	Ph-BT	—
OH	1688.372	−0.40	0.000	0.20	Ph-BT	Fe, Th
OH	1688.913	−0.30	0.000	0.18	Ph-BT	Fe
OH	1689.087	−0.40	0.000	0.18	Ph-BT	—
OH	1689.978	−0.40	0.000	0.23	Ph-BT	Fe
OH	1690.339	−0.30	0.000	0.25	Ph-BT	Fe
OH	1690.891	−0.40	0.000	0.23	Ph-BT	—
OH	1691.027	−0.40	0.000	0.18	Ph-BT	—
OH	1691.388	−0.50	0.014	0.23	Ph-BT	—
OH	1695.517	−0.20	0.000	0.10	Ph-BT	—
OH	1700.910	−0.60	0.022	0.09	Ph-BT	Th
OH	1705.688	−0.20	0.000	0.20	Ph-BT	Fe
OH	1707.077	−0.40	0.000	0.17	Ph-BT	—
OH	1710.109	−0.40	0.017	0.19	Ph-BT	—
OH	1710.440	−0.60	0.010	0.18	Ph-BT	—
OH	1710.942	−0.30	0.017	0.23	Ph-BT	—
OH	1711.181	−0.40	0.000	0.18	Ph-BT	—
OH	1717.982	−0.12	0.044	0.11	Ph-BT	—
OH	1732.697	−0.20	0.000	0.20	Ph-BT	—
OH	1733.871	−0.30	0.000	0.17	Ph-BT	Fe
OH	1734.501	−0.66	0.048	0.17	Ph-BT	—
OH	1735.167	−0.26	0.049	0.22	Ph-BT	—
OH	1741.871	−0.39	0.037	0.16	Ph-BT	—
OH	1762.373	−0.30	0.000	0.15	Ph-BT	—
OH	1777.190	−0.10	0.000	0.15	Ph-BT	—
OH	1781.951	−0.10	0.000	0.17	Ph-BT	—
OH	1783.556	−0.41	0.022	0.10	Ph-BT	—
OH	1828.562	−0.05	0.050	0.24	Ph-BT	—

B. FULL SPECTRUM COMPARISON

Full wavelength comparison of Barnard's star spectrum against a synthetic model with a $T_{\rm eff}$ of 3200 K, [M/H] of -0.5, and $\log g$ of 5 dex.

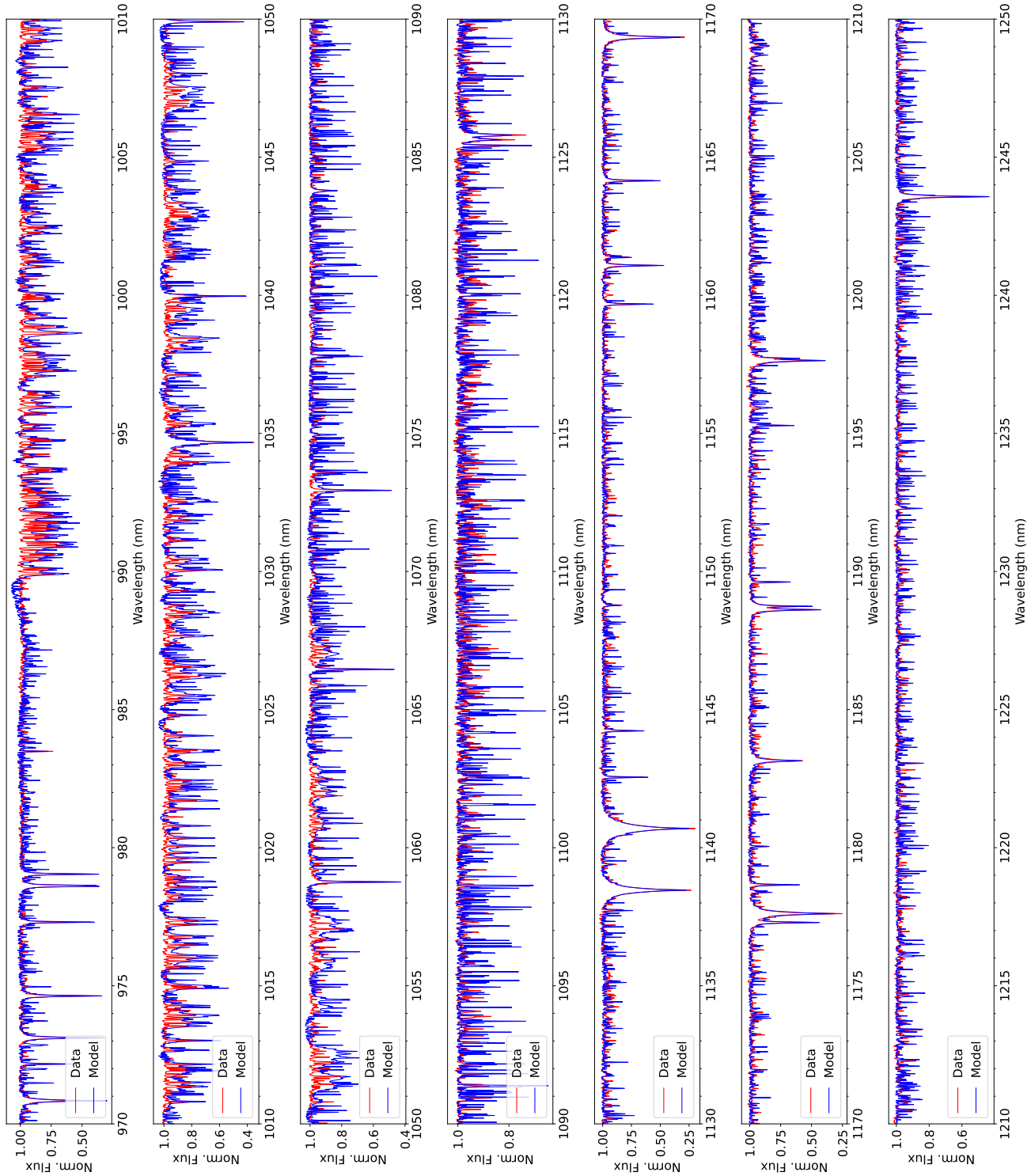

Figure B.1. Comparison between the observed data (red) and the model (blue) with $T_{\rm eff}$, $\log g$, and metallicity of 3200 K, 5.0 dex and -0.5 dex, respectively. The continuum mismatch (see Section 3.1.1) is evident within 985-1068 nm.

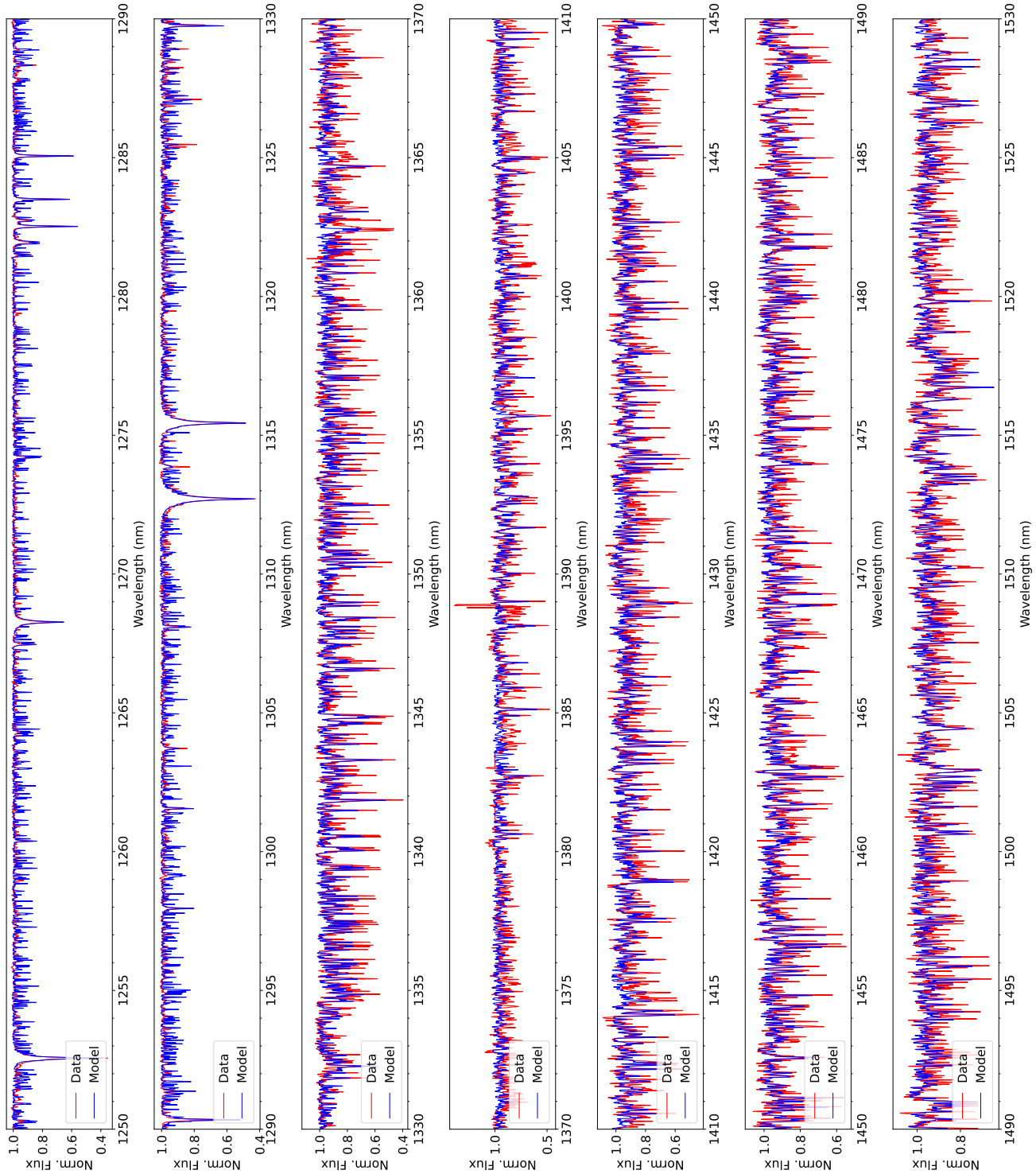

Figure B.2. Comparison between the observed data (red) and the model (blue) with $T_{\rm eff}$, $\log g$, and metallicity of 3200 K, 5.0 dex and −0.5 dex, respectively.

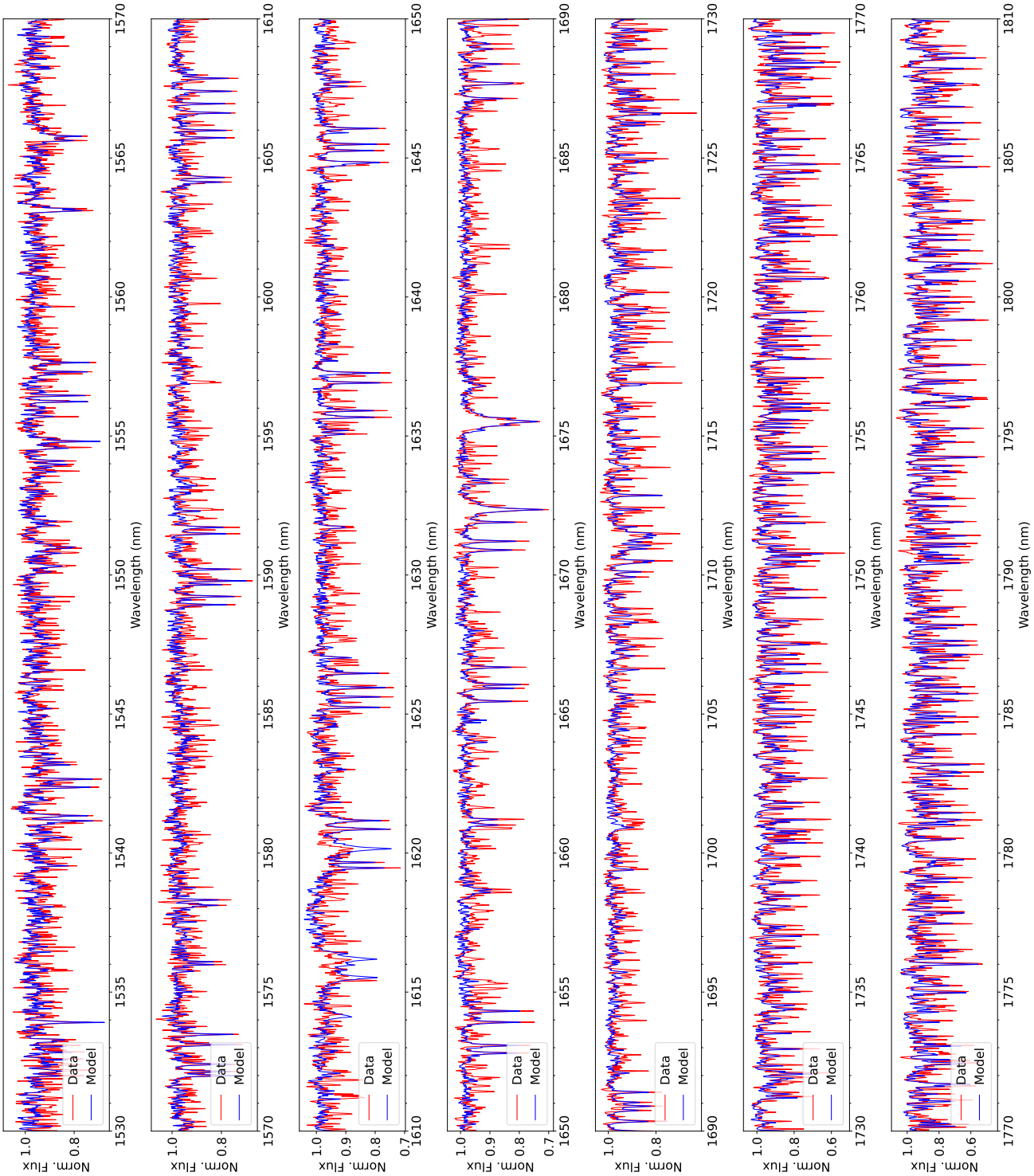

Figure B.3. Comparison between the observed data (red) and the model (blue) with $T_{\rm eff}$, $\log g$, and metallicity of 3200 K, 5.0 dex and −0.5 dex, respectively.

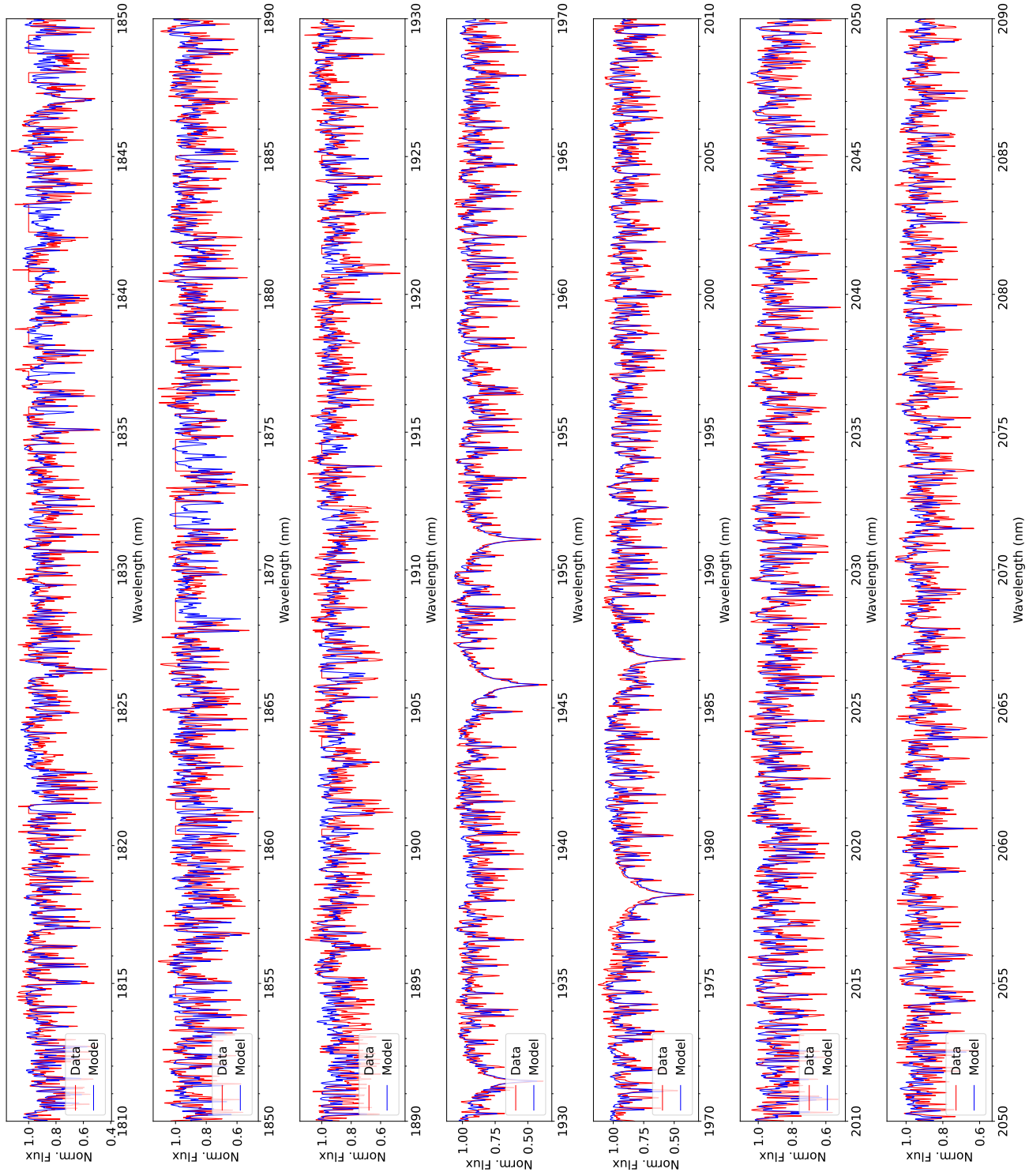

Figure B.4. Comparison between the observed data (red) and the model (blue) with $T_{\rm eff}$, $\log g$, and metallicity of 3200 K, 5.0 dex and −0.5 dex, respectively. The missing data in locations such as 1840 nm are due to the telluric corrections.

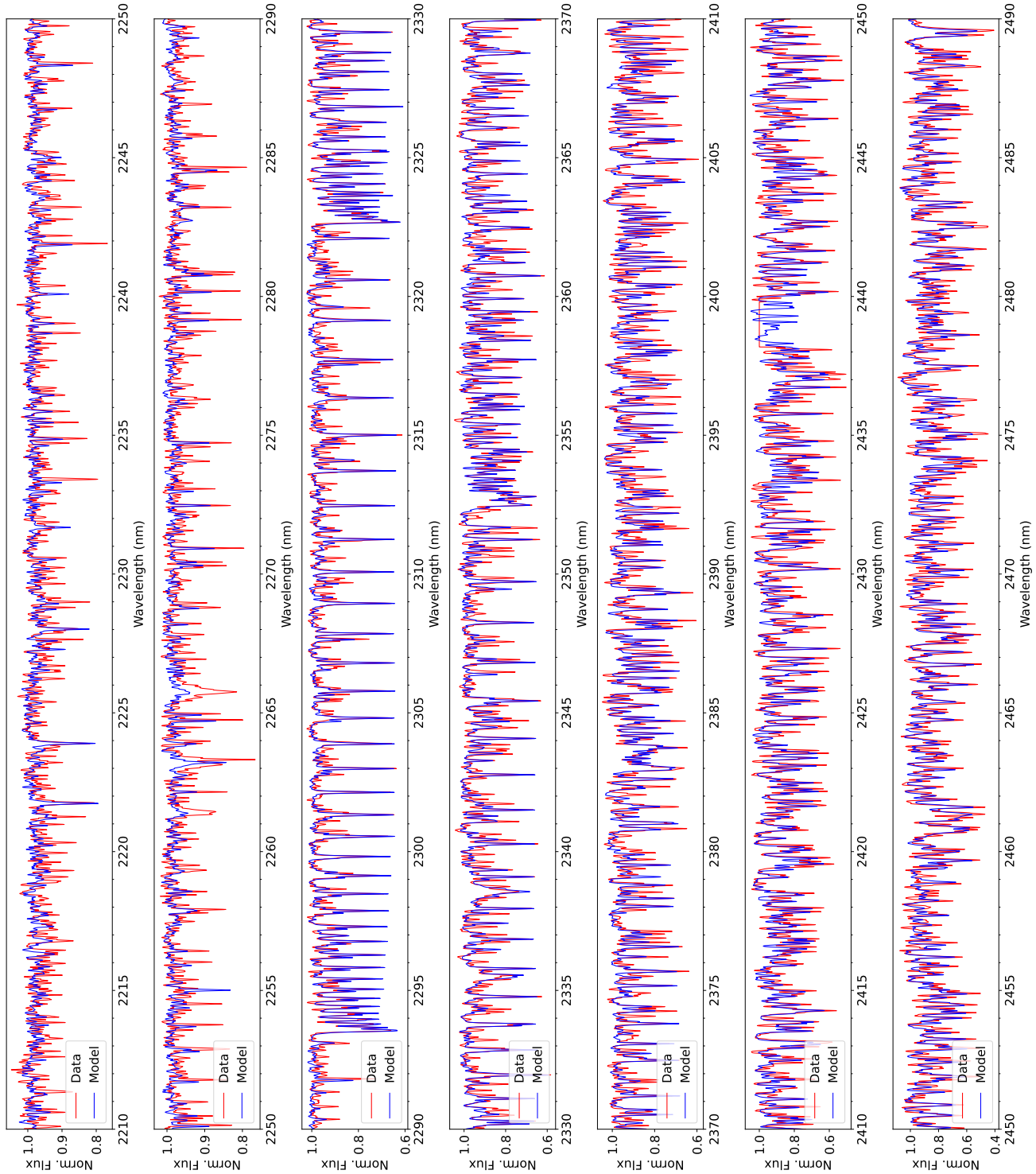

Figure B.5. Comparison between the observed data (red) and the model (blue) with $T_{\rm eff}$, $\log g$, and metallicity of 3200 K, 5.0 dex and −0.5 dex, respectively.